Xue et al. *Microsystems & Nanoengineering* (2026)12:321
https://doi.org/10.1038/s41378-026-01436-5

Microsystems & Nanoengineering
www.nature.com/micronano

ARTICLE Open Access

A mechanically robust wearable sweat analysis platform with plug-and-play interconnects for continuous biomarker profiling

Tianhao Xue[1], Wanting Lin[1], Jiahui Zhou[1], Chaodan Luo[1], Bohua Li[1], Xiaofang Zhang[2], Ching-Jung Chen[3]✉, Jen-Tsai Liu[4] and Guixian Zhu[1]✉

Abstract

Reliable electromechanical integration between disposable soft sensors and rigid hardware is crucial for wearable devices, yet physically fragile interfaces often cause severe motion artifacts and contact failures during exercise. To overcome this challenge, this study presents a mechanically robust sweat analysis platform featuring plug-and-play interconnects. Diverging from vulnerable printed inks, a scalable Flexible Printed Circuit Board (FPCB) was engineered with Electroless Nickel Immersion Gold (ENIG) terminals reinforced by a 0.1-mm Polyimide (PI) stiffener. This design ensures highly stable metal-to-metal contact under physical strain. To mitigate chloride corrosion while maintaining the high geometrical consistency of ENIG finishes, a hierarchical architecture was developed utilizing surface-modified carbon as the electrochemical transducer. The system enables accurate detection of lactate (5–80 mM, 0.04046 μA/mM), Na^+ (12.5–200 mM, 119.59 mV/decade), and equivalent impedance-based sweat rate (< 0.23 μL/min). Crucially, these robust interconnects facilitated 51 min of uninterrupted monitoring during vigorous aerobic and anaerobic exercises. Based on the acquired data, a proof-of-concept framework mapping sweat rate against lactate concentration was established for personalized exercise intensity zoning, offering a mass-manufacturable paradigm for precision sports physiology.

Introduction

Wearable sweat sensing systems have garnered significant attention in recent years[1–8]. Sweat, as an easily accessible biofluid, contains not only water but also a variety of physiological biomarkers, such as electrolytes (Na^+, K^+), metabolites (lactate, urea), and proteins[6,9,10]. The concentration changes of these components can reflect the physiological state, providing critical insights for health monitoring[11–13]. For instance, the detection of chloride concentration in sweat has been established as the gold standard for diagnosing cystic fibrosis[14–16]. However, the application of sweat detection in exercise monitoring is particularly noteworthy. Lactate levels serve as a key indicator for evaluating athletes' aerobic and anaerobic capacities, offering valuable insights for optimizing training intensity and recovery strategies[11,17–19]. Previous studies have shown that sweat lactate can increase during exercise and that the sweat lactate threshold is correlated with the blood lactate threshold[20]. Additionally, the levels of ions and sweat rate can be used to assess hydration status and the severity of fluid loss, thereby enhancing athletic performance and preventing dehydration risks[21–23]. In particular, sweat Na^+ concentration and sweat rate can be combined to estimate sweat Na^+ loss and fluid loss, which is important for guiding fluid/electrolyte replacement during exercise[24]. Therefore, the development of a wearable device capable of real-time, continuous monitoring of multiple biomarkers in sweat holds significant importance for exercise

Correspondence: Ching-Jung Chen (cjchen@ucas.ac.cn) or Guixian Zhu (zhuguixian@bistu.edu.cn)
[1]School of Instrument Science and Optoelectronic Engineering, Beijing Information Science and Technology University, Beijing, China
[2]Department of Clinical Laboratory, Tianjin Medical University General Hospital, Tianjin, China
Full list of author information is available at the end of the article

science. By accurately monitoring physiological changes during exercise, athletes can better design training programs, improve performance, and reduce the risk of sports-related injuries.

Electrochemical sensing technology has become the mainstream method for detecting sweat biomarkers due to its high sensitivity and selectivity[25–29]. Recent advances in large-area integrated sensing and computing devices have demonstrated the importance of scalable fabrication, device-level uniformity, and system-level integration for next-generation intelligent devices[30–32]. However, the transition from laboratory prototypes to reliable wearable products is severely hindered by unstable electromechanical integration. Currently, most flexible sensors rely on laser etching[3,33,34], inkjet printing[2,35,36], and screen printing[8,37,38]. While these methods are effective for fabricating sensing arrays, connecting these soft substrates to rigid hardware lacks standardized specifications. Conventional connections, such as mechanical clamps or conductive adhesives, are physically fragile and prone to disconnection. During intense physical exercise, continuous skin deformation often leads to poor electrical contact at these interfaces. Furthermore, the printed conductive inks can easily crack or peel off under interface friction. Ultimately, these issues cause extreme fluctuations in contact resistance and massive motion artifacts, directly compromising the reliability of continuous physiological monitoring.

To address the physical fragility of conventional soft sensors, Flexible Printed Circuit Board (FPCB) technology has emerged as a robust alternative. As a flexible evolution of traditional Printed Circuit Boards (PCBs), FPCB retains established industrial manufacturing capabilities while utilizing a compliant polyimide (PI) substrate. This architecture introduces mature industrial interface engineering to achieve highly reliable electromechanical connections. In circuit manufacturing, a widely adopted surface finish is Electroless Nickel Immersion Gold (ENIG). The ENIG process deposits a robust nickel diffusion barrier topped with a thin immersion gold layer over the copper traces, providing an exceptionally flat, highly conductive, and oxidation-resistant surface. For electromechanical integration, these ENIG-plated pads are commonly designed as parallel “gold fingers”. Because the flexible substrate is prone to buckling during hardware connection, a localized stiffener—typically a rigid PI plate—is routinely laminated to the back of the gold finger region. This structural reinforcement precisely adjusts the thickness of the flexible tail, transforming it into a robust insertion plug. Consequently, it enables a simple but secure connection with standard receptacles, creating a highly stable metal-to-metal contact. Importantly, this architecture enables a mechanically stable and reusable electrical interface between the disposable sensing front-end and the wearable electronic module.

Beyond providing a stable physical interface, benefiting from standardized electronic manufacturing, PCB/FPCB architectures have also been widely utilized as highly reliable electrochemical sensing electrodes. Existing literature firmly establishes their viability for high-performance analysis. For instance, Dutta et al. developed a commercially fabricated Lab-on-PCB electrochemical glucose sensor, achieving a 10 μM–9 mM detection range (10 μM limit of detection in static conditions), with sensitivity improving at higher flow rates[39]. Liu et al. achieved the detection of 10 mM–160 mM Na^+ and 1 mM–16 mM K^+ using a PCB-based ion-selective electrode, with the initial potential deviation of Na^+ and K^+ sensors after repeated tests eliminated by 20 and 40 mV, respectively[40]. Notably, Mansor et al. reported that gold-coated PCB sensors exhibited superior quasi-reversible electrochemical behavior and higher charge transfer resistance compared to flexible PET-based counterparts[41]. Nandeshwar et al. developed a low-cost ENIG-finished PCB electrochemical sensor for myeloperoxidase (MPO) detection in blood plasma, with a limit of detection of 15.79 ng/mL[42].

Building upon these combined mechanical and electrochemical advantages, this study proposes a scalable, multi-modal wearable platform to address the critical need for continuous exercise physiology monitoring. While the pristine ENIG interface provides an exceptionally consistent and highly conductive geometric template, the direct exposure of these standard gold surfaces to chloride-rich sweat inevitably leads to chemical corrosion[43]. To resolve this conflict between geometric precision and chemical vulnerability, a hierarchical electrode architecture is introduced. Specifically, the photolithographically defined ENIG layer functions strictly as a current collector, while a surface-modified carbon layer serves as the electrochemical transducer, effectively shielding the underlying gold. By combining this sensing front-end with microfluidic sweat collection technology, a dual two-electrode detection system featuring a shared reference electrode was developed. This configuration ensures reliable signal transmission from the soft sensing interface to the integrated potentiostat chip, which serves as the electrochemical core of the hardware. Consequently, the system enables the simultaneous monitoring of multiple biomarkers: lactate via chronoamperometry (CA), Na^+ via open-circuit potential (OCP), and sweat rate via equivalent impedance analysis. Furthermore, relying on the continuous data acquired through these metal-to-metal interconnects, a proof-of-concept framework correlating sweat rate with lactate concentration is demonstrated. By identifying individual physiological thresholds

rather than relying on generic population standards, this method offers a novel perspective for personalized exercise intensity zoning. Ultimately, this work not only expands the application of FPCB in wearable sensing but also establishes a scalable technical pathway for the mass manufacturing of precision sports physiology monitors.

Experimental section

Chemicals and materials

Lactate, Glutaraldehyde, Prussian blue, Sodium chloride (NaCl), Tetrahydrofuran (THF), Poly(vinyl chloride) (PVC), Ascorbic acid, Urea, Calcium chloride anhydrous ($CaCl_2$), Magnesium chloride hexahydrate ($MgCl_2$), Ammonium chloride, 99.5% (NH_4Cl) were obtained from Innochem (Beijing, China). Glucose, Potassium chloride (KCl), Ethanol, Tetraethyl 4-tert-Butylcalix[4]arene-O,O',O",O"'-tetraacetate (Sodium ionophore X), Bis(2-ethylhexyl) sebacate (DOS), Sodium tetrakis[3,5-bis(trifluoromethyl)phenyl]borate were obtained from Aladdin (Shanghai, China). Lactate Oxidase was obtained from Psaitong (Beijing, China). Uric acid was obtained from Macklin (Shanghai, China). Distilled water was obtained from Hunan BKMAN Holding Co., Ltd. Artificial sweat (ISO 3160-2 standard, pH 7.4) was purchased from Shanghai Yuanye Bio-Technology Co., Ltd. Carbon-Prussian blue ink was obtained from Guangdong Silver Well Trading Co., Ltd., model number C2070424P2. Carbon ink was obtained from LOCTITE, model number LOCTITE EDAG 423ss. Silver/silver chloride ink was obtained from Shanghai Julong Electronic Technology Co., Ltd., model number JLL-20. Artificial sweat (ISO 3160-2 standard, pH 7.4) was purchased from Shanghai Yuanye Bio-Technology Co., Ltd.

Microchannel design and simulation

The microchannel structure was designed using AutoCAD and exported as an STL format file. The simulation of sweat flow behavior in the serpentine channel and arc collection zone was conducted using Fluent 2023. Before the simulation, the microchannel model was imported into ICEM CFD software for meshing, and the mesh file was subsequently imported into Fluent 2023 for simulation. Since the primary component of sweat is water (accounting for 99%), water was selected as the simulation medium. In the VOF (Volume of Fluid) simulation, the inlet flow rate with a radius of 1 mm was set to 0.25 μL/min, and the inlet flow rate with a radius of 2 mm was set to 1 μL/min. Transient simulations were performed at different time intervals.

Fabrication of the microchannel patch

The fabrication of the microchannel patch was carried out using the MAKEX M-One Pro 30 DLP (Digital Light Processing) 3D printer, with the M-FC model of flexible material employed for printing. Initially, the microchannel model designed in AutoCAD was imported into the MAKEX supporting software, with the shrinkage rate set to 99.65%, layer thickness to 20 μm, light intensity to medium, and exposure time to 4.5 s. After printing, the printing platform was cleaned with ethanol. Since the cured material is not dissolved by ethanol, the microchannel patch remained intact and was thoroughly cleaned. Subsequently, the ethanol on the surface of the patch was blown dry using nitrogen, and the patch was further cured for 3 min using a UV curing lamp.

Device characterization

All electrochemical measurements were conducted using a Chi 660E electrochemical workstation. Scanning electron microscopy imaging was performed on a CIQTEK DB550 FIB-SEM. High-precision multimeter measurements were carried out using a FLUKE 116 C model. The voltage source employed was an ATTEN TPR32-5A model, with a voltage output accuracy of 0.01 V. The soldering station used was an ATTEN 8865 model.

Electrochemical measurement conditions

Unless otherwise specified, all in vitro electrochemical measurements were conducted under controlled room-temperature conditions of 25 ± 2 °C. These measurements included cyclic voltammetry, chronoamperometric lactate sensing, open-circuit potential measurements for Na^+ sensing, and impedance-related characterization. The sensors and test solutions were allowed to equilibrate to room temperature before measurement. For on-body exercise measurements, the experiments were performed in an indoor environment at approximately 26 ± 3 °C, and the participant was allowed to acclimate to the testing environment before data collection.

Electrochemical measurement parameters

For cyclic voltammetry (CV) characterization of FPCB electrode reproducibility, the initial potential was −0.6 V, with upper and lower vertex potentials of 0.6 V and −0.6 V, respectively. The final potential was set to 0 V. The initial scan polarity was negative, the scan rate was 0.1 V/s, the sampling interval was 0.001 V, the quiet time was 2 s, and the number of scan segments was 8. For CA lactate sensing, the initial potential was 0 V, and the detection potential was set to −0.3 V. The initial step polarity was negative, the pulse width was 60 s, the sampling interval was 0.003 s, and the quiet time was 0 s. The current response was used to quantify lactate concentration. For OCP measurement of Na^+, the measurement time was 60 s, and the sampling interval was 0.1 s. The high and low potential limits were set to 1 V and −1 V, respectively. The OCP response was used to quantify Na^+ concentration.

Hydrophilic treatment

The microchannel patch was subjected to hydrophilic treatment using Huaxia Jiahe Q100 hydrophilic nanocoating. The specific procedure was as follows: a pipette gun was used to precisely dispense the hydrophilic coating onto the areas requiring treatment (e.g., sweat inlet, serpentine channel, and arc collection zone). The coated patch was then left to stand at room temperature for 24 h, allowing the coating to completely dry and form a stable hydrophilic surface.

Fabrication of sensing electrodes

The Voltera Nova High Performance & Maskless Flexible Microelectronics Printer was employed for the precise deposition of electrode materials on FPCB substrates. Carbon ink and silver/silver chloride ink were accurately dispensed onto the working and reference electrodes, respectively, utilizing the printer's advanced capabilities, including a probe accuracy of <3 μm, an optimal line width of <100 μm, and an alignment precision of 100 μm. The process parameters were configured as follows: print speed 120 mm/min, dispense pressure 5000, minimum raise height 5 μm, dispense threshold 50%, nozzle diameter 50 μm, print height 75 μm, relief pressure 4000, and pre-temperature 25 °C. For material selection, a Prussian blue -free carbon ink was used for the sodium ion working electrode, while a Prussian blue-containing carbon ink was applied to the lactate working electrode. Following deposition, a two-stage drying protocol was implemented: initial curing at 72 °C for 30 min, succeeded by an increase to 121 °C for an additional 30 min. This methodology ensured precise material application and effective curing, thereby establishing a robust foundation for consistent electrochemical performance.

Fabrication of lactate sensor

A 5 wt% aqueous solution of glutaraldehyde (1.3 μL/mm²) was dispensed onto the working electrode and allowed to dry at room temperature for 1 h. Subsequently, a solution of lactate oxidase with a concentration of 1 KU/ml (1.6 μL/mm²) was applied to the working electrode and left to dry at room temperature for 1.5 h.

Fabrication of sodium sensor

A mixture consisting of 1 wt% Na^+ ionophore X, 0.55 wt % sodium tetrakis[3,5-bis(trifluoromethyl)phenyl] borate ion exchanger, 33 wt% PVC, and 65.45 wt% DOS was prepared, with a total mass of 100 mg. Subsequently, the mixture was completely dissolved in 660 μL of THF to form a homogeneous solution for the Na^+ selective electrode. The prepared solution was then uniformly drop-cast onto the surface of the Na^+ working electrode (1.3 μL/mm²) and left to stand at room temperature for 2 h to form a uniform Na^+ selective membrane. Finally, 40 μL of a solution containing 100 mM Na^+ was evenly applied to the surface of the Na^+ sensor and incubated at room temperature for 1 h.

On-body measurement methods

For aerobic and anaerobic sweat sensing, the participant wore the device on their wrist, with FPCB electrochemical sensing electrodes and microfluidic channels adhered to the skin. Data collection began approximately 5 min (aerobic) and 9 min (anaerobic) after the start of exercise. During aerobic exercise, the participant first completed 13 min of activity, followed by 5 min of stretching and rest, then performed 22 min of aerobic exercise, ending with 11 min of stretching and rest. For anaerobic exercise, the participant completed 15 min of initial activity, followed by 5 min of stretching and rest, then performed 13 min of anaerobic exercise, followed by 12 continuous minutes of anaerobic activity, concluding with 6 min of stretching and rest. Sweat lactate and sodium ion concentrations were recorded every minute, while sweat rate and body temperature were sampled every 3 min. Data was collected through the customized APP. Origin was used for data analysis and visualization, including graph plotting, data calculations, and extraction of relevant parameters.

Results and discussion

Schematic diagram of the multimodal wearable sweat sensing system

Figure 1 illustrates the overall schematic of a wearable sweat biochemical indicator detection system. The device assesses aerobic/anaerobic exercise by analyzing sweat biomarkers. The principle and design are shown in Fig. 1a. The system uses a microfluidic patch to collect sweat samples. It incorporates FPCB sensing electrodes for monitoring Na^+, lactate concentrations and sweat flow rate. The device is also equipped with a BLE module, enabling connectivity with the customized APP for visual data analysis and convenient management. Figure 1b presents the sensing front-end of the system. The layered schematic of the sensing front-end is depicted in Fig. 1b (i), showing the structure from top to bottom: the FPCB-based electrochemical Sensing Electrode, Microchannel, and Skin, with a 5-pin magnetic connector on the right. Figure 1b (ii) details the FPCB-based electrochemical sensing electrode, which features a substrate treated with ENIG surface modification. The electrode is divided into three parts. The upper section features a serpentine impedance detection area made up of two parallel curved conductive lines connected to the leftmost two pins. This area measures sweat equivalent impedance to analyze the sweat flow rate. The middle section, the electrochemical detection area, contains three circular electrodes. The left and right ones act as working electrodes for Na^+ and

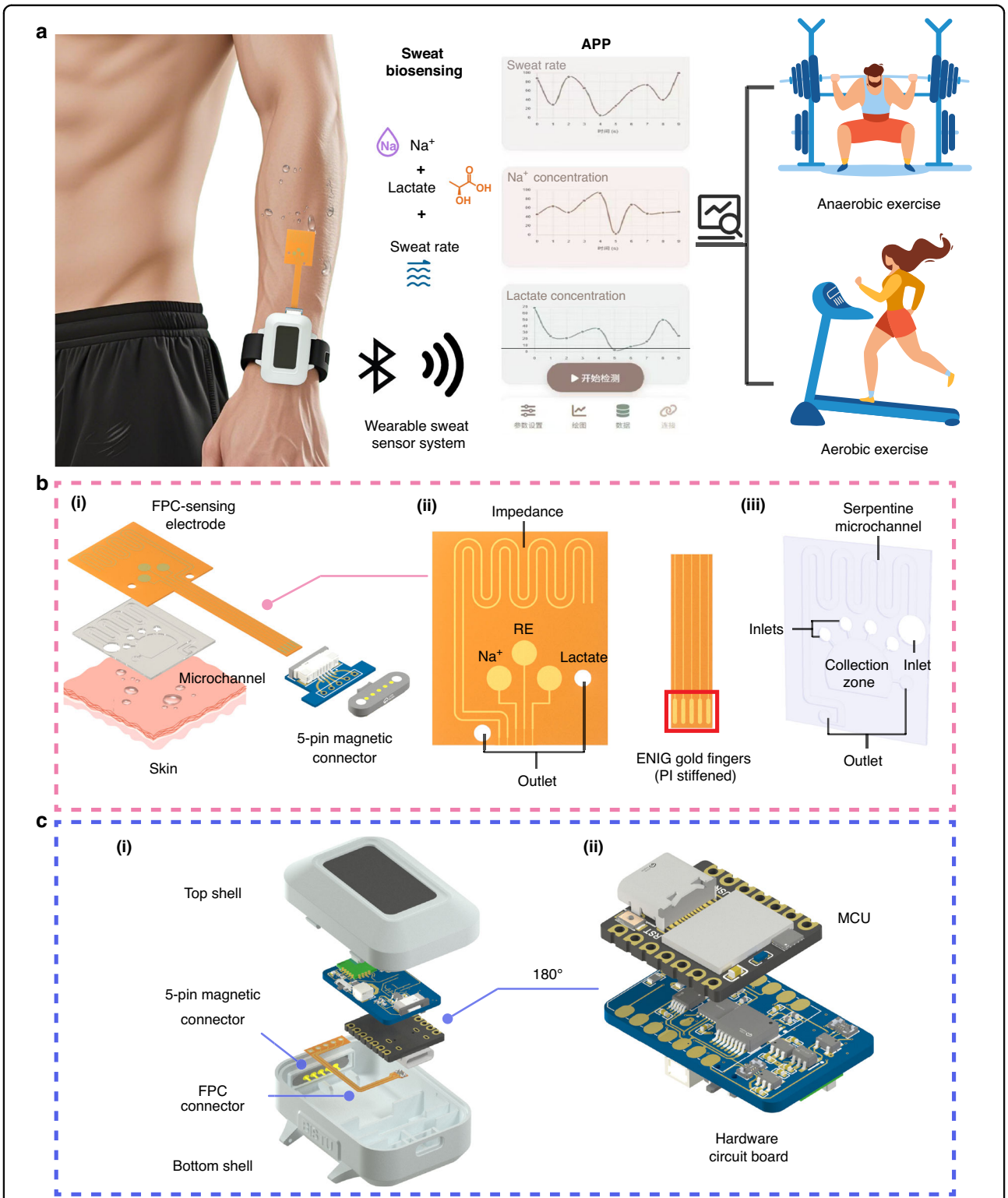

Fig. 1 Schematic diagram of the overall system for sweat biochemical signal detection based on FPCB. a Principle and design of the overall device. **b** Composition of the sensing front-end. (i) Layered schematic of the sensing front-end. (ii) FPCB-based electrochemical sensor. (iii) Flexible microfluidic patch fabricated via light-curing 3D printing. **c** Composition of the hardware system. (i) Layered schematic of the hardware system. (ii) Schematic of the core hardware circuit board and MCU

lactate detection, respectively, while the center upper electrode serves as a common reference electrode. The electrochemical sensing electrode is based on an FPCB, and the three circular electrodes are connected to the rightmost three electrochemical pins. To establish a highly reliable electromechanical link with the hardware, the terminal end of the FPCB is laminated with a rigid PI stiffener. This structural reinforcement transforms the flexible PI tail into a robust "gold finger" insertion plug. Unlike fragile conductive adhesives or printed inks, this rigid-flex architecture provides a highly stable, low-impedance physical interface that easily withstands repeated mating cycles. After post-processing and electrochemical modification, they form a dual two-electrode electrochemical detection system. The lower section includes sweat outlets, corresponding to the outlets of the microfluidic patch, for discharging collected sweat. The sensing electrode integrates equivalent impedance detection and electrochemical analysis through optimized structural design.

The microfluidic patch, fabricated via light-curing 3D printing, is shown in Fig. 1b (iii). The size and shape of the microfluidic patch correspond to the FPCB electrochemical sensing electrode. The patch consists of a Serpentine Microchannel, Sweat Collection Zone, inlets, and outlets from top to bottom. The Serpentine Microchannel collects sweat for equivalent impedance measurement, while the Sweat Collection Zone gathers sweat for electrochemical detection. Sweat enters the system through designated inlets. A single 2-mm-radius inlet directs sweat into the serpentine microchannel for flow rate measurement. Meanwhile, an array of four 1-mm-radius central inlets guides sweat into the main collection zone for electrochemical analysis. The two outlets on the microchannel align in size and position with the outlets on the FPCB sensing electrode for discharging collected sweat. Figure 1c depicts the hardware system of the device. Figure 1c (i) and Fig. 1c (ii) show the layered schematic and the core circuit (MCU, Hardware circuit board) of the hardware system, respectively. The layered schematic illustrates the structure from top to bottom: Top Shell, Hardware Circuit Board, MCU (Seeed Studio XIAO nRF52840), FPC Connector, and Bottom Shell. The hardware system connects to the sensing front-end via a 5-pin magnetic interface, enabling a detachable sensor design that enhances user convenience.

Characterization of the FPCB electrochemical sensor

FPCB technology provides a standardized and commercially scalable platform for constructing flexible electrochemical electrodes. Under the IPC-6013B framework, the electrode patterns, conductive traces, and connection terminals are fabricated through mature industrial processes, including photolithography, etching, surface finishing, and lamination. These standardized processes allow accurate control of the electrode area, trace width, and terminal spacing. Compared with manual patterning or low-resolution printing, the FPCB process can reduce device-to-device geometric variation and improve fabrication consistency. In addition, FPCB fabrication is suitable for array-based production, where multiple sensing electrodes can be processed on the same flexible substrate under identical manufacturing conditions. The ENIG surface finish provides a uniform metal contact region, while the PI stiffener reinforces the connection tail for reliable plug-in integration. These features support reproducible fabrication and standardized integration of the FPCB sensing electrodes with wearable electronics.

Unlike traditional screen-printed electrodes (SPES) limited by mesh resolution, the underlying ENIG layer is defined by photolithography, serving as a high-precision geometric template and current collector with a standard immersion gold thickness of 2 μ" (0.05 μm). To prevent the inevitable chloride-induced corrosion of bare gold during sweat analysis, a carbon-based interfacial layer was strategically introduced over the working electrodes. This intermediate layer acts simultaneously as an electrochemical transducer and a hermetic barrier. As illustrated in the layered modification diagrams (Fig. 2a), this hierarchical architecture is specifically tailored for each target analyte: For the common reference electrode, Ag/AgCl ink is deposited directly onto the pristine ENIG surface. For the Na^+ working electrode, a plain carbon paste layer shields the ENIG substrate, followed by the coating of a Na^+-selective membrane to enable highly specific potentiometric detection via the OCP method. For the lactate working electrode, the protective carbon matrix is doped with Prussian blue, acting as an efficient electron mediator to facilitate redox charge transfer. Subsequently, an enzymatic membrane comprising lactate oxidase and glutaraldehyde is cross-linked onto this transducer, ensuring robust specificity for amperometric detection. In this configuration, the carbon ink ensures excellent conductivity, while the enzyme layer guarantees high specificity. Figure 2b (i) shows the EDS layered image of ENIG (500× magnification), and Fig. 2b (ii) presents the electron image of ENIG (500× magnification). The EDS spectrum, shown in Fig. S1, indicates a mass fraction of 62.4% Ni and 37.6% Au. Detailed elemental analysis and additional EDS layered images can be found in Table S1 and Fig. S2.

The FPCB electrochemical sensor was designed using EDA software and fabricated through a standard FPCB manufacturing process. This digital design workflow allows the electrode geometry, trace routing, terminal spacing, and array layout to be readily modified by updating the layout file. After design modification, the revised layout can be directly transferred to the industrial FPCB fabrication process without preparing a new screen

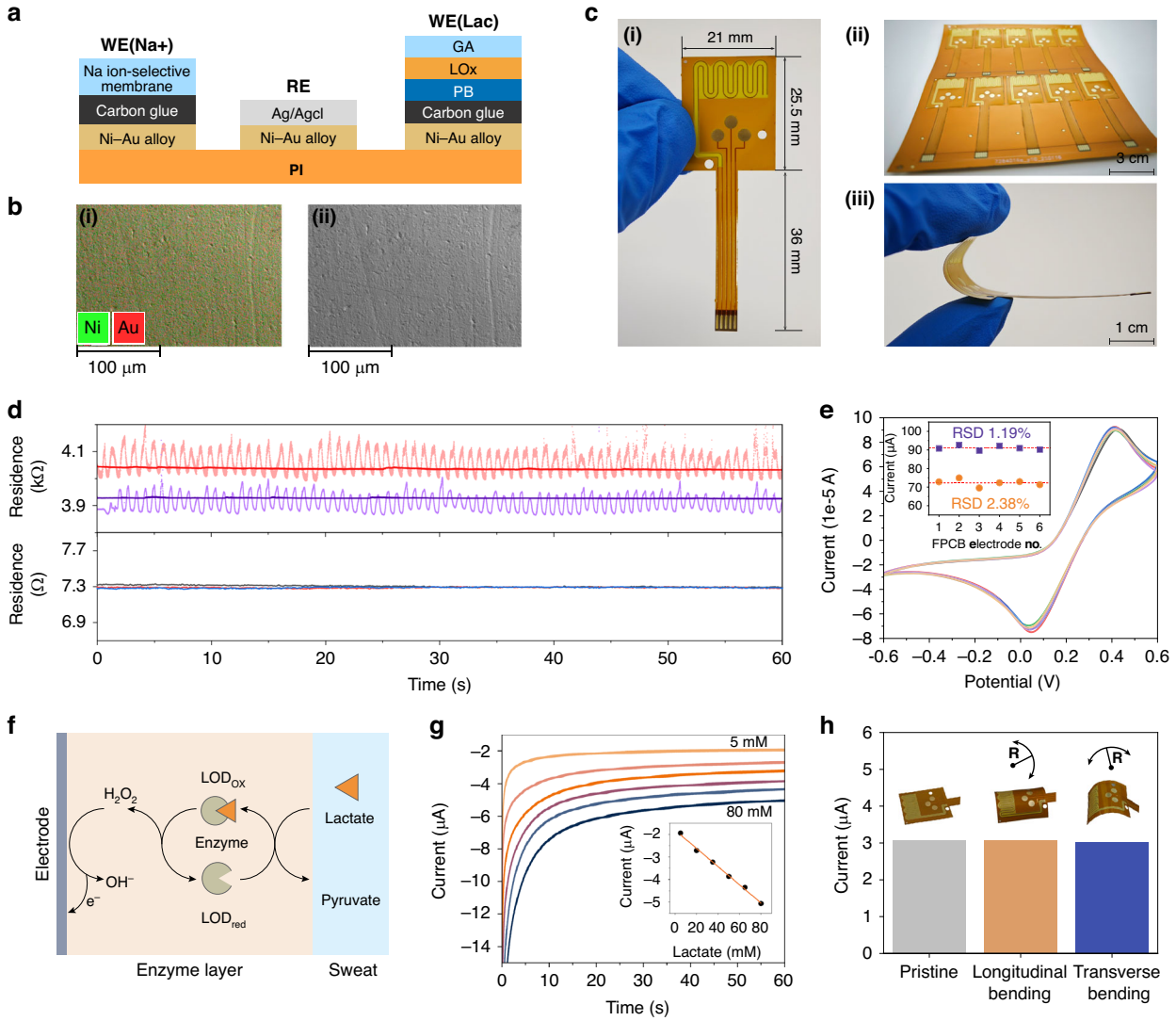

Fig. 2 Modification and characterization of the FPCB electrochemical sensor. a Schematic of the layered structure of the FPCB electrochemical sensor with Na^+ and lactate sensing electrodes. **b** (i) EDS layered image of ENIG (500× magnification). (ii) Electron image of ENIG (500× magnification). **c** Physical images of the FPCB electrochemical sensing electrode. (i) Shape and dimensions of a single FPCB electrochemical sensing electrode. (ii) FPCB electrochemical sensing electrode array designed and fabricated using EDA software. (iii) Bendability of the FPCB electrochemical sensing electrode. **d** Comparison of dynamic contact resistance between the SPE (top) and FPCB electrode (bottom) during continuous bending. The FPCB completely eliminates the severe motion artifacts and >4 kΩ internal resistance observed in the SPE, ensuring a highly stable electromechanical interface even after repeated mating cycles. **e** CV curves of six different FPCB electrodes in a mixed solution of 5 mM potassium ferricyanide, 5 mM potassium ferrocyanide, and potassium nitrate. Inset: Oxidation peak currents (blue) and reduction peak currents (orange) (absolute values) of six FPCB electrodes, along with their RSD. **f** Reaction mechanism of lactate sensing using CA. **g** CA current responses of the lactate sensing electrode in lactate solutions with concentrations of 5 mM, 20 mM, 35 mM, 50 mM, 65 mM, and 80 mM (fixed potential: −0.3 V). Inset: Linear fitting results of current values corresponding to different lactate concentrations. **h** Current at the last second (absolute values) of the same lactate sensing electrode under unbent, longitudinal bending, and transverse bending conditions (lactate concentration: 50 mM, fixed potential: −0.3 V). **i** Eight repeated CA tests of the same lactate sensing electrode under identical conditions (test duration: 60 s, lactate concentration: 50 mM, fixed potential: -0.3 V), showing current values and relative responses (normalized to the mean of eight measurements). **j** Fitting curves of four lactate sensing electrodes modified under the same conditions, tested in lactate solutions ranging from 5 mM to 80 mM (fixed potential: −0.3 V). Inset: Sensitivity (slope) and RSD of the four electrodes. **k** Anti-interference performance of the lactate sensing electrode (baseline solution: 35 mM lactate, fixed potential: −0.3 V). **l** Reaction mechanism of Na^+ sensing using OCP. **m** OCP voltage responses of the Na^+ sensing electrode in NaCl solutions with concentrations of 12.5 mM, 25 mM, 50 mM, 100 mM, and 200 mM. Inset: Linear fitting results of voltage values corresponding to different NaCl concentrations. **n** OCP tests of the same Na^+ sensing electrode under unbent, longitudinal bending, and transverse bending conditions (Na^+ concentration: 50 mM). **o** Nineteen repeated OCP tests of the same Na^+ sensing electrode under identical conditions (test duration: 60 s, NaCl concentration: 50 mM), showing voltage values and relative responses (normalized to the mean of 19 measurements). **p** Fitting curves of four Na^+ sensing electrodes modified under the same conditions, tested in NaCl solutions ranging from 12.5 mM to 200 mM. Inset: Sensitivity (slope) and RSD of the four electrodes. **q** Anti-interference performance of the Na^+ sensing electrode

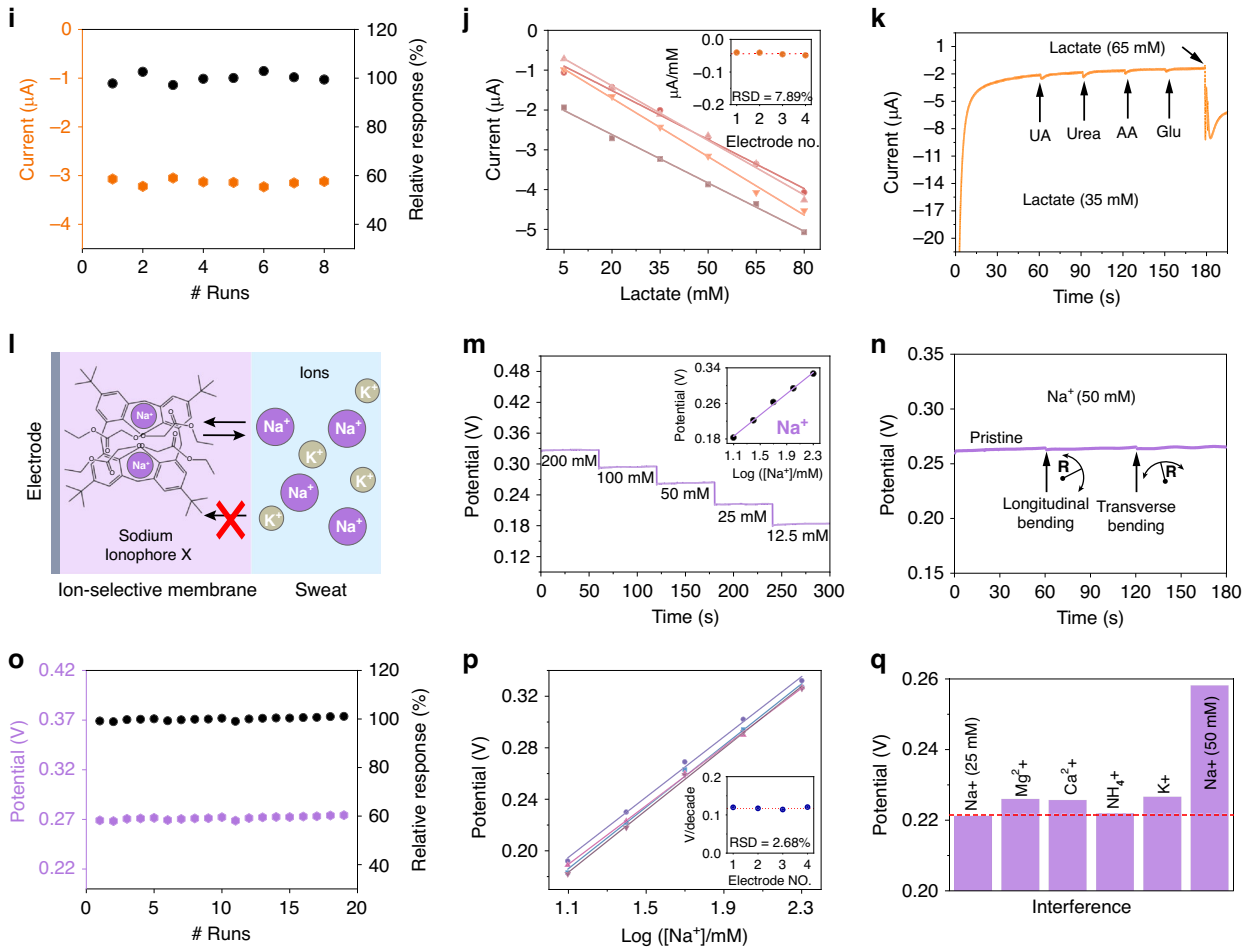

Fig. 2 (Continued.)

or mask for each design iteration. Figure 2c displays the physical image of the FPCB electrochemical sensor. Figure 2c (i) shows the shape and dimensions of a single FPCB electrochemical sensor, with the sensing section measuring 21 mm in width and 23 mm in length, and the lower pins measuring 36 mm in length. The sensor has five pins with a spacing of 1 mm between them. More detailed dimensions are provided in Fig. S3, which includes annotations for the working and reference electrodes, pin sizes, wire lengths and widths, and sweat outlet dimensions. Figure 2c (ii) shows the FPCB electrochemical sensor array, with detailed dimensions, including the number of electrodes, electrode sizes, spacing, and array dimensions, provided in Fig. S4. The array-format layout further demonstrates that multiple identical sensing electrodes can be designed and fabricated simultaneously on a shared flexible substrate panel, which is beneficial for improving fabrication throughput and reducing device-to-device geometric variation. Figure 2c (iii) demonstrates the bendability of FPCB, which, due to its flexible nature, allows it to conform closely to the skin, meeting the requirements of wearable devices. The above array-format fabrication also provides potential advantages for practical production and cost reduction. Multiple FPCB sensing front-ends can be fabricated together in one batch, which may improve fabrication efficiency and reduce the cost of each replaceable sensing unit at larger production scales. In addition, the sensing front-end can be replaced after use, while the electronic module can be reused. This separated design may further reduce the cost per measurement in practical use.

To experimentally validate the mechanical superiority of the rigid-flex interconnects under dynamic strain, continuous contact resistance was monitored during electrode bending (Fig. 2d). Prior to testing, the sensing regions of both electrode types were short-circuited using conductive silver paste to ensure identical measurement conditions. The detailed electromechanical connection configurations for both electrode types are visually presented in Figure S5. As depicted in the top panel of Fig. 2d, traditional SPE (SUNJEEN D-SPE 301) exhibited an inherent baseline resistance exceeding 4 kΩ. While

stable in a stationary state, the SPEs exhibited clear resistance variations corresponding to the up-and-down bending motions. More critically, this dynamic process was accompanied by catastrophic motion artifacts, with transient resistance spiking drastically (visually demonstrated in Supplementary Video S1). As further detailed in the expanded-scale relative fluctuation plot (Fig. S6), the motion-induced resistance error of the SPEs could even exceed 100%. Notably, after just a single insertion-extraction cycle (red curve), the severity of these motion-induced spikes exacerbated significantly. In stark contrast, the FPCB electrode (Fig. 2d, bottom) demonstrated an ultra-low inherent resistance of 7.3 Ω. Crucially, whether during the initial insertion (black curve) or after repeated mating cycles (blue curve), the FPCB maintained an exceptionally flat and stable electrical interface during continuous bending (see Supplementary Video S2 for real-time monitoring).

The plugging/unplugging durability of the interface was further evaluated over 1–300 cycles. As shown in Fig. S7, the SPE interface exhibited progressively more visible mechanical wear with increasing cycle number, whereas the FPCB interface only showed minor localized indentation marks after repeated contact. The corresponding resistance evolution is summarized in Fig. S8. The contact resistance of the FPCB interface remained highly stable, changing only slightly from 7.3 Ω to 7.2 Ω over 300 cycles. In contrast, the SPE interface remained at the kΩ level throughout the test. These results demonstrate the superior interconnection stability of the FPCB-based plug-and-play structure under 1–300 plugging/unplugging cycles, fully validating its reliability for repeated use scenarios. Further statistical analyzes of measurement errors are detailed in Fig. S9.

To further evaluate the stability of the FPCB electrode under sweat-related conditions, the FPCB electrode was immersed in artificial sweat (pH 7.4) prepared according to the ISO 3160-2 standard. The artificial sweat contained NaCl, NH_4Cl, urea, acetic acid, and lactic acid, with the pH adjusted to 7.4 using NaOH. As shown in Fig. S10, no obvious macroscopic corrosion, delamination, or structural damage was observed after immersion for 12 h. The small marks on the electrode surface were caused by the multimeter probe during resistance measurement, rather than corrosion after artificial sweat immersion. The resistance values measured at five representative positions, including two serpentine conductive traces and three electrochemical electrodes, remained nearly unchanged during the immersion test (Table S2), suggesting that the FPCB electrode maintained electrical continuity under the tested artificial sweat condition. It should be noted that this test only evaluated the short-term stability of the FPCB electrode in artificial sweat at pH 7.4. Real sweat may have different pH values and compositions. Therefore, longer-term reliability under more complex wearing and sweat-exposure conditions still requires further evaluation. Considering the possible influence of chloride ions in sweat, the carbon layer on the working electrode and the Ag/AgCl layer on the reference electrode remain necessary for stable electrochemical sensing.

To systematically evaluate the electrochemical reproducibility of the FPCB sensors, cyclic voltammetry (CV) tests were conducted in a mixed electrolyte system containing 5 mM potassium ferricyanide, 5 mM potassium ferrocyanide, and potassium nitrate. The tests used an external Ag/AgCl reference electrode, with a potential scan range of −0.6 V to 0.6 V, a sampling interval of 0.001 s, and a scan rate of 0.1 V/s. Each electrode underwent four CV scans. Figure 2e shows the CV curves of the last scan for six FPCB electrodes. The curves are highly overlapping, indicating consistent electrochemical behavior among different electrodes. The inset summarizes the oxidation and reduction peak currents (absolute values) obtained from the six electrodes. The oxidation peak current, shown in dark blue, exhibited a relative standard deviation (RSD) of 1.19%, while the reduction peak current, shown in orange, showed an RSD of 2.38%. These low RSD values further confirm that the standardized FPCB fabrication process enables reproducible electrode geometry and stable electrochemical responses, which are important for scalable production and reliable calibration of wearable sensing electrodes. The complete four scans are shown in Fig. S11, and the detailed oxidation and reduction peak voltages and currents of the six FPCB electrodes are provided in Table S3. Together with the stable electromechanical connection demonstrated above, these results show that the FPCB platform provides both interface reliability and electrochemical reproducibility for wearable sweat sensing.

Figure 2f illustrates the reaction mechanism of lactate CA sensing. Lactate oxidase is immobilized on the electrode surface, catalyzing the reaction of lactate with oxygen to produce pyruvate and hydrogen peroxide (H_2O_2). Prussian blue efficiently reduces H_2O_2, releasing electrons (e^-) and generating a current signal. The CA response of the lactate sensor at a fixed potential of −0.3 V in lactate solutions with concentrations is shown in Fig. 2g. The sensor demonstrates excellent linearity (calibration curve: $y = -0.04046x - 1.81057$, $R^2 > 0.99$) across a concentration range of 5 mM to 80 mM, covering the typical lactate concentration range in human sweat[11,44].

To evaluate the impact of bending on the sensor, CA tests were conducted on the same lactate sensor in a 50 mM lactate solution under unbent, longitudinal bending (radius of curvature: 1 cm), and transverse bending conditions (radius of curvature: 1 cm). The

absolute current values of the last second are shown in Fig. 2h. The results show that bending does not significantly affect the steady-state CA current value. Figure 2i demonstrates the repeatability of the lactate sensor, with eight CA tests conducted under the same conditions (60 s test time, 50 mM lactate solution). The current values and relative responses (normalized to the mean of eight measurements) are recorded. The experimental results demonstrate a measured current of −3.14 μA ± 0.09 μA, with relative responses consistently maintained at approximately 100%, reflecting exceptional reproducibility across repeated experimental trials. Figure 2j shows the fitting curves of four lactate sensors modified under the same conditions, tested in lactate solutions ranging from 5 mM to 80 mM. The four fitting curves are highly consistent. The inset displays the sensitivity (slope) of the four sensors, with an RSD of 7.89%, indicating high consistency among the lactate sensors. Table S4 provides the CA data for the four lactate sensors, including current values and sensitivities at different concentrations. Figure 2k evaluates the anti-interference performance of the FPCB-based lactate sensor using CA. The baseline is established in a 35 mM lactate solution, with interference substances added at 60 s (0.5 mM uric acid), 90 s (10 mM urea), 120 s (0.5 mM ascorbic acid), and 150 s (1 mM glucose). Finally, 65 mM lactate is added at 180 s. The results show that the current signals remain stable when interference substances are added. Only high-concentration lactate causes significant changes, demonstrating the sensor's excellent anti - interference to common sweat components.

Figure 2l illustrates the working principle and calibration curve of Na^+ sensing, using valinomycin (ionophore X) in the sodium ion-selective membrane for selective Na^+ recognition. OCP measurement results are presented in Fig. 2m, where the Na^+ sensor demonstrates high sensitivity to changes in Na^+ concentration. The sensor demonstrates excellent linearity (calibration curve: $y = 0.11959x + 0.05462$, $R^2 > 0.99$) across the 12.5 mM to 200 mM concentration range, fully encompassing the typical Na^+ concentration range in human sweat (15 mM to 70 mM)[45]. Figure 2n evaluates the impact of bending on the Na^+ sensor, with OCP measurements conducted in a 50 mM NaCl solution under unbent, longitudinal bending (radius of curvature: 1 cm), and transverse bending (radius of curvature: 1 cm) conditions. The results show no significant effect of bending on the OCP voltage response. Figure 2o demonstrates the repeatability of the Na^+ sensor, with 19 OCP tests conducted under the same conditions (60 s test time, 50 mM Na^+ solution). The voltage values and relative responses (normalized to the mean of 19 measurements) are recorded. The results show an OCP of 0.27 V ± 2.96 mV, with relative responses maintaining a stable range within proximity to 100%, demonstrating high reproducibility and consistency across repeated experiments. Figure 2p shows the repeatability test results of different Na^+ sensors, with four sensors modified under the same conditions tested in NaCl solutions ranging from 12.5 mM to 200 mM. The inset displays the sensitivity (slope) of the four sensors, with an RSD of 2.68%, indicating high consistency among the Na^+ sensors. Table S5 provides the OCP data for the four Na^+ sensors, including voltage values and sensitivities at different concentrations. Figure S12 provides detailed characterization of the four Na^+ sensors at different concentrations, including fitting curves with error bars (Fig. S12a), box plots of OCP distributions (Fig. S12b), and RSD calculations of OCP at different concentrations (Fig. S12c). Na^+ selectivity tests (Fig. 2q) were conducted by measuring OCP responses in 10 mM NaCl (background), followed by sequential addition of interfering ions (5 mM KCl, 5 mM NH_4Cl, 0.5 mM $MgCl_2$, 0.5 mM $CaCl_2$). A final 10 mM NaCl addition confirmed Na^+-specific response.

Testing and characterization of microchannels

Figure 3 illustrates the testing and characterization of the microfluidic patch. This design employs a microfluidic channel patch fabricated using a light-curing 3D printer, featuring intricate microstructures. The 3D model of the microfluidic patch is shown in Fig. 3a, where Fig. 3a (i) presents the front view schematic and Fig. 3a (ii) presents the back view schematic. The patch adopts a dual-functional zone design, dedicated to equivalent impedance measurement and electrochemical detection of sweat, respectively. Specifically, the patch consists of a serpentine channel and an arc-shaped sweat collection zone: the serpentine channel is primarily responsible for collecting sweat for equivalent impedance measurement, while the arc-shaped zone collects sweat samples for electrochemical detection. The patch surface is equipped with five sweat inlets, including four 1 mm-radius inlets for electrochemical detection and one 2 mm-radius inlet for equivalent impedance measurement. Notably, the total area of the four small inlets equals that of the single large inlet, ensuring consistent sweat intake efficiency for both detection methods. Detailed dimensions and parameters of the microfluidic patch can be found in Fig. S13. Figure 3b (i) shows a physical image of the microfluidic patch. Figure 3b (ii) further demonstrates the patch's bendability, as it is made of flexible material that can undergo varying degrees of deformation under different external forces. This flexible design ensures that the patch can conform closely to the skin surface, providing a comfortable wearing experience while enabling efficient sweat collection.

Figure 3c presents a side view of the microfluidic patch combined with the FPCB sensing electrode. The patch has

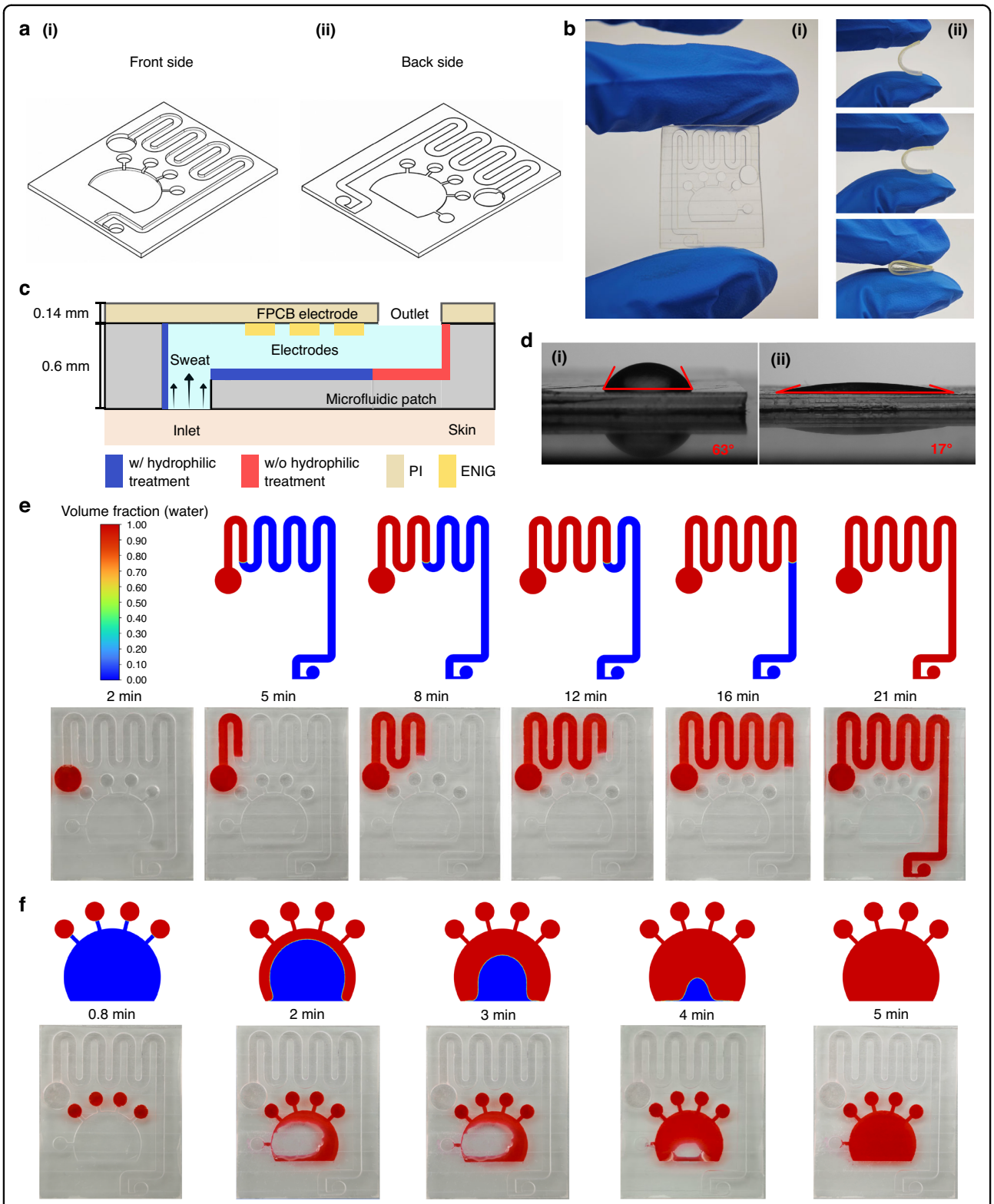

Fig. 3 Testing and characterization of microchannels and flow performance. a 3D model of the microchannel patch. (i) Schematic of the front view of the microchannel patch. (ii) Schematic of the back view of the microchannel patch. **b** (i) Physical image of the microchannel patch, showing its physical structure and design details. (ii) Images of the patch at different bending angles, demonstrating its flexibility. **c** Side view of the microchannel patch, including detailed dimension annotations. The process of sweat collection is also illustrated. **d** Contact angles on the patch surface. (i) Contact angle on the patch surface before hydrophilic coating treatment. (ii) Contact angle on the patch surface after hydrophilic coating treatment. **e** Comparison of simulation results and experimental results for sweat filling in serpentine microchannels. **f** Comparison of simulation results and experimental results for sweat filling in the sweat collection zone

an overall thickness of 0.6 mm, with the serpentine channel height at 0.4 mm and the arc-shaped collection zone height at 0.15 mm. The inlets of the microfluidic patch are designed to be fully open, allowing direct collection of sweat secreted from the skin. The outlets align with those of the FPCB electrochemical electrode, forming a "bottom-in, top-out" sweat collection mechanism: the outlets expel air when the microchannels are not filled with sweat and expel sweat once the channels are full. To optimize sweat flow performance, the inlets, serpentine channel, and arc-shaped collection zone were treated with a hydrophilic coating, while the outlets remained untreated to ensure sweat fully fills the channels and collection zone before being expelled. The side view clearly shows the hydrophilic-treated regions, while Fig. S14 provides a top-down view with detailed annotations. The blue areas indicate hydrophilic-treated inlets, serpentine channel, and arc-shaped collection zone, while red areas indicate untreated outlets. This zonal treatment design effectively guides the directional flow of sweat, ensuring collection efficiency. Figure 3d presents contact angle test results, verifying the effectiveness of the hydrophilic treatment. As shown in Fig. 3d (i), the untreated patch has a contact angle of 63°. In Fig. 3d (ii), after hydrophilic treatment, the contact angle significantly decreases to 17°, indicating a substantial improvement in surface hydrophilicity.

Figure 3e shows the simulation results of the patch, with the sweat intake rate set at 0.5 μL/min for the 1 mm-radius inlet and 2 μL/min for the 2 mm-radius inlet, resulting in a total intake rate of 2 μL/min for the four inlets. The serpentine channel has a total capacity of 41.8 μL, while the arc-shaped collection zone has a capacity of approximately 9.67 μL. The simulation results demonstrate that the microfluidic patch effectively facilitates sweat flow and collection in the serpentine channel, with the serpentine channel taking about 21 min to fill and the arc-shaped zone taking about 5 min. The experimental results of the filling process in the serpentine channel are shown in Fig. 3f, and those for the arc-shaped collection zone are shown in Fig. 3g. The experimental results closely match the simulation results, validating the feasibility and accuracy of the design. These findings indicate that the design performs well in sweat collection and flow control, providing a reliable basis for the practical application of the microfluidic patch.

Although the microfluidic patch provided directional sweat collection and transport in experiments, several potential error sources should still be considered during practical use. In the current design, hydrophilic patterning (Fig. S14) was used to guide sweat transport and facilitate directional flow in the microchannel. However, at low sweating rates, sweat renewal in the channel may be slow, which can increase the response delay and make the measured biomarker concentration more susceptible to local evaporation. At high sweating rates, rapid flow may shorten the residence time of sweat in the sensing region and, under extreme conditions, may cause overflow or unstable sampling. In addition, bubbles, dust, and skin debris may partially block the microchannel or inlet, leading to discontinuous sweat transport and possible detection errors. These effects may influence the accuracy of sweat flow rate estimation and biomarker concentration measurement. Future work will further improve the microfluidic sampling reliability by using a more enclosed low-evaporation structure, anti-blocking inlet design, and flow-rate calibration under different sweating conditions.

Characterization of the hardware system

The performance of the hardware system determines the reliability of the sensing backend. Figure 4a illustrates the specific shape and dimensions of the hardware system, with a comparison to a coin for size reference. The block diagram of the hardware system in Fig. 4b outlines the acquisition pathways and processing flow for biochemical. The electrochemical signals are transmitted to the potentiostat chip (LMP91000), while the equivalent impedance signals are sent to the impedance measurement chip (AD5933). Subsequently, the data is transferred to the MCU, which then transmits the signals via BLE to a custom-developed mobile application. The APP enables real-time data display and graphical visualization. Figure 4c demonstrates the OCP method for electrochemical detection of Na^+ in sweat. Figure 4d illustrates the CA method for electrochemical detection of lactate in sweat, whereby CA measures the current to determine the lactate concentration. Fig. 4e presents the method for measuring sweat equivalent impedance. Sensor 1 and Sensor 2 represent the two serpentine traces in the equivalent impedance measurement region, connected to two electrode interfaces. When sweat flows into the serpentine channel, it comes into contact with the two traces. The more sweat in the channel, the lower the equivalent impedance between the two traces. By precisely measuring the equivalent impedance of the channel using electrochemical impedance analysis, the volume of sweat in the channel can be indirectly determined before the serpentine channel for impedance measurement is fully filled. Dividing this sweat volume by the duration of the test yields the sweat secretion rate.

Due to the small amplitude of the collected signals such as voltage and current, the measurement accuracy of the hardware system is crucial. Therefore, it is essential to comprehensively verify the accuracy of the hardware system's OCP, CA and impedance measurement functions. The OCP performance verification involves applying a known fixed voltage to the OCP pins using a calibrated voltage source. The hardware system's output

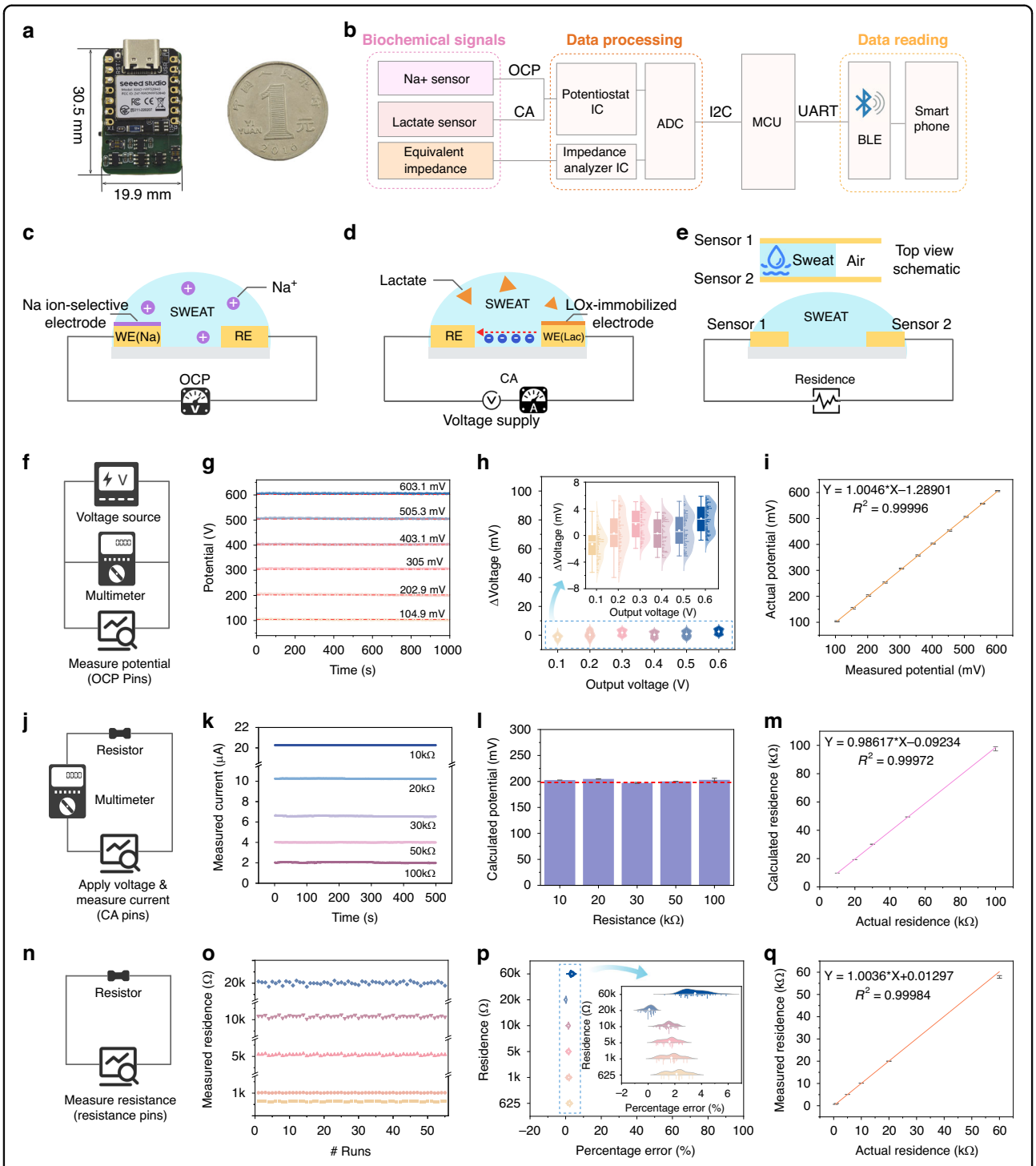

Fig. 4 (See legend on next page.)

values are then read via a serial port and compared with high-precision multimeter measurements to assess accuracy and stability. (Fig. 4f). For OCP performance verification, the voltage source output ranges from 0.1 V to 0.6 V (with a step size of 0.05 V). The voltage source output pins are connected to the OCP measurement pins of the device, and the voltage read by the device is output via the serial port at a rate of one data point per second. Each voltage is tested for 1000 s. Simultaneously, a high-precision multimeter is connected to the voltage source

(see figure on previous page)

Fig. 4 Performance characterization of the hardware system. a The physical dimensions of the hardware system (compared to a one-yuan coin for size reference). **b** A system-level block diagram illustrating the signal conversion, processing, and wireless transmission from biochemical signal sensors to the user interface. **c** Schematic diagram of the electrochemical detection method for sweat Na^+ using OCP. **d** Schematic diagram of the electrochemical detection method for sweat Na^+ using CA. **e** Schematic diagram of the sweat impedance detection method. **f** Functional validation and measurement methodology of the OCP mode in the hardware system. **g** Comparison of voltage values measured by the hardware system over 1000 seconds at different potentials versus the actual applied voltage values measured by a high-precision multimeter. The red dashed line represents the actual voltage values, while the solid line represents the measured voltage values. **h** Box plot of the voltage difference (ΔVoltage) between the measured and actual voltages within the applied voltage range of 0.1 V to 0.6 V. **i** Linear fitting of the average values from 1000 measurements by the hardware system versus the true values measured by the multimeter, with applied voltages ranging from 0.1 V to 0.6 V in 0.05 V increments. **j** Functional validation and measurement methodology of the CA mode in the hardware system. **k** Current values measured over 500 seconds by the hardware system in CA mode with a fixed applied voltage of 198 mV, while varying the resistance connected to the CA pin. **l** Comparison of the voltage derived from the measured current and actual resistance versus the fixed voltage of 198 mV. The orange dashed line represents 198 mV. **m** Linear fitting of the resistance values calculated from the measured current (198 mV / measured current) versus the actual resistance values. **n** Functional validation and measurement methodology of the impedance measurement mode in the hardware system. **o** Scatter plot of the hardware system's impedance measurement results across different load impedance levels (620 Ω, 1 kΩ, 5 kΩ, 10 kΩ, and 20 kΩ) (sample size, n = 55). **p** Percentage error of the hardware system's impedance measurements under different load impedance conditions. **q** Linear fitting of the impedance values measured by the hardware system versus the actual resistance values

output pins to record the actual output voltage, which serves as the true data. When the voltage source outputs 0.1 V, 0.2 V, and 0.3 V, the actual output voltages measured by the multimeter are 104.9 mV, 202.9 mV, and 305 mV, respectively. When the voltage source outputs 0.4 V, 0.5 V, and 0.6 V, the actual output voltages measured by the multimeter are 403.1 mV, 505.3 mV, and 603.1 mV, respectively. Figure 4g shows the comparison between the voltage values measured by the hardware system over 1000 s and the actual applied voltage values at these six voltages. The red dashed line in the figure represents the actual voltage values, while the solid line represents the voltage values measured by the hardware system. Figure 4h presents a box plot analysis of the deviation between 100 sets of measured data and the true voltage values. The horizontal line in the plot indicates the median of the deviations, and the circles represent the mean distribution. The maximum deviation is 6.31 mV, occurring at the 0.2 V measurement point, with a calculated maximum relative error of 5.24%. Table S6 lists the complete voltage measurement values for the OCP verification of the hardware system, including the mean, standard deviation, maximum, and minimum values for voltages from 0.1 V to 0.6 V (with a step size of 0.05 V). The 1000 data points for each voltage from 0.1 V to 0.6 V (with a step size of 0.1 V) are averaged every 10 points, resulting in 100 data points per voltage. Figure 4i shows the linear fitting of the average of 1000 measurements by the hardware system against the true voltage values measured by the multimeter for applied voltages ranging from 0.1 V to 0.6 V (with a step size of 0.05 V). The fitting curve equation is $y = 1.0046x - 1.28901$, achieving a linearity of $R^2 > 0.99$, indicating a strong linear relationship between the measured values and the true voltage values, thus verifying the accuracy of the OCP measurement.

Figure 4j illustrates the functional verification and measurement method for CA. The CA performance verification involves connecting the CA pins of the device to a resistor to measure the loop current, which is then output via the serial port. The current measurement values output by the hardware system should match the theoretically calculated values (applied voltage/resistance), thereby verifying the accuracy of the CA measurement. Therefore, the CA performance verification is conducted in two ways: the first method involves fixing the applied voltage and changing the resistance connected to the CA pins to measure the loop current, verifying the effect of load resistance variation on the loop current; the second method involves fixing the resistance connected to the CA pins and changing the applied voltage to measure the loop current, verifying the effect of applied voltage variation on the loop current. The voltage applied to the CA pins of the hardware system can be modified via the microcontroller's internal code. Figure 4k shows the variation in the loop current measured over 500 s at a fixed voltage of 198 mV with resistances of 10 kΩ, 20 kΩ, 30 kΩ, 50 kΩ, and 100 kΩ connected to the CA pins. By comparing the measured current values with the calculated current values (fixed voltage/resistance), the accuracy of the current measurement can be determined. The maximum percentage error of the CA current measurement is calculated to be 2.46%. Table S7 lists the complete current measurement data for the CA verification of the hardware system with a fixed voltage of 198 mV applied to the CA pins. In addition to comparing the currents, the applied voltage can be inversely calculated (measured current * resistance) and compared with 198 mV. In Fig. 4l, the orange dashed line represents 198 mV, showing that the calculated voltages for different resistances are consistent with 198 mV. Figure 4m shows the linear fitting of the calculated resistance values (198 mV/

Table 1 Power consumption of the wearable device under different operating modes

Operating mode	Recording time	Min current	Max current	Average current	Estimated power
BLE advertising	20 min	12.8 mA	13.9 mA	13.2 mA	48.8 mW
BLE connected without sensing	20 min	12.6 mA	12.8 mA	12.7 mA	47.0 mW
Continuous sensing and BLE transmission	20 min	9.1 mA	15.4 mA	13.5 mA	50.0 mW

measured current) against the actual resistance values. The fitting curve equation is $y = 0.98617x - 0.09234$, achieving a linearity of $R^2 > 0.99$, indicating a strong linear relationship between the calculated resistance values and the true resistance values.

Figure 4k, Fig. 4l, and Fig. 4m comprehensively verify the accuracy of the CA measurement of the hardware device from the perspectives of current, voltage, and resistance. The loop current can also be measured by fixing the resistance and changing the applied voltage. Figure S15 specifically shows the data measured when the voltage is changed and the resistance is fixed at 20 kΩ. Figure S15a and Figure S15b show the current responses measured by the hardware device under forward and reverse bias, respectively. Table S8 lists the complete current measurement data for the CA verification of the hardware system with a fixed resistance of 20 kΩ and varying voltages applied to the CA pins. The "Actual Voltage (mV)" in the table is the voltage across the CA pins measured by the high-precision multimeter. The resistance can be calculated (applied voltage/measured current) from the measured current and the actual applied voltage. Figure S15c shows the comparison between the measured resistance and the actual 20 kΩ resistance, with the dashed line representing the actual resistance value. Figure S15d shows the linear fitting of the voltage values inversely calculated from the current and the 20 kΩ resistance against the actual applied voltage. The fitting curve equation is $y = 0.99234x + 9.61081$, achieving a linearity of $R^2 > 0.99$.

To validate the equivalent impedance detection function of the hardware system, this study employs standard resistors as references, characterizing its performance through resistance measurements. As shown in Fig. 4n, the measurement method involves connecting known resistors to the two pins of the impedance sensing device, reading the resistance values via the serial port, and comparing them with the actual resistance values to assess measurement accuracy. First, the measurement conditions are determined based on the range of equivalent impedance. According to the capacitive measurement results of artificial sweat in the serpentine channel in Fig. S16, under a 200 Hz AC voltage and a flow rate of 2 μL/min, the capacitance reaches a maximum value of 0.807 μF at 1250 s, indicating that the channel is fully filled with 41.8 μL of artificial sweat. Using the equivalent impedance calculation formula:

$$X_C = \frac{1}{2\pi f C} \tag{1}$$

the maximum equivalent impedance is calculated to be 986.6 Ω, corresponding to the minimum capacitive reactance. Therefore, the minimum equivalent resistance value (620 Ω) selected for the verification experiment is lower than this value. Additionally, based on the 41.8 μL of artificial sweat corresponding to 0.807 μF capacitance, 1 μL of artificial sweat corresponds to 19.31 nF capacitance, resulting in an equivalent impedance of 41.25 kΩ at 200 Hz. To ensure the device's resolution for sweat volume is less than 1 μL, the maximum measured resistance value should exceed 41.25 kΩ. At this frequency, an equivalent impedance of 60 kΩ corresponds to a capacitance of 13.26 nF, approximately equivalent to 0.69 μL of sweat volume. Thus, selecting 60 kΩ as the upper limit ensures the device's resolution for sweat volume is less than 0.69 μL. Furthermore, by calculating the proportional relationship between the device's detection area and the area of human sweating skin, the overall sweat secretion during exercise can be estimated. This method provides a reliable quantitative basis for assessing body fluid loss during exercise or in high-temperature environments. Figure 4o shows the measurement results of the hardware system for resistances of 620 Ω, 1 kΩ, 5 kΩ, 10 kΩ, and 20 kΩ at 200 Hz (the scatter plot for the 60 kΩ resistance is presented in Fig. S17). Each resistance is measured 55 times, and the data points are tightly clustered, indicating high repeatability. Figure 4p further illustrates the percentage measurement error under different load impedance conditions. The results show that within the range of 620 Ω to 60 kΩ, the maximum percentage error of the equivalent impedance measurement of the hardware system is 5.89%, verifying the high precision of the equivalent impedance measurement. Notably, since the system is calibrated using a 20 kΩ resistor, the measurement error is minimized and most concentrated at this impedance value. Table S9 lists the complete resistance measurement values for the impedance verification of the hardware system, including the mean, standard deviation, maximum, and minimum

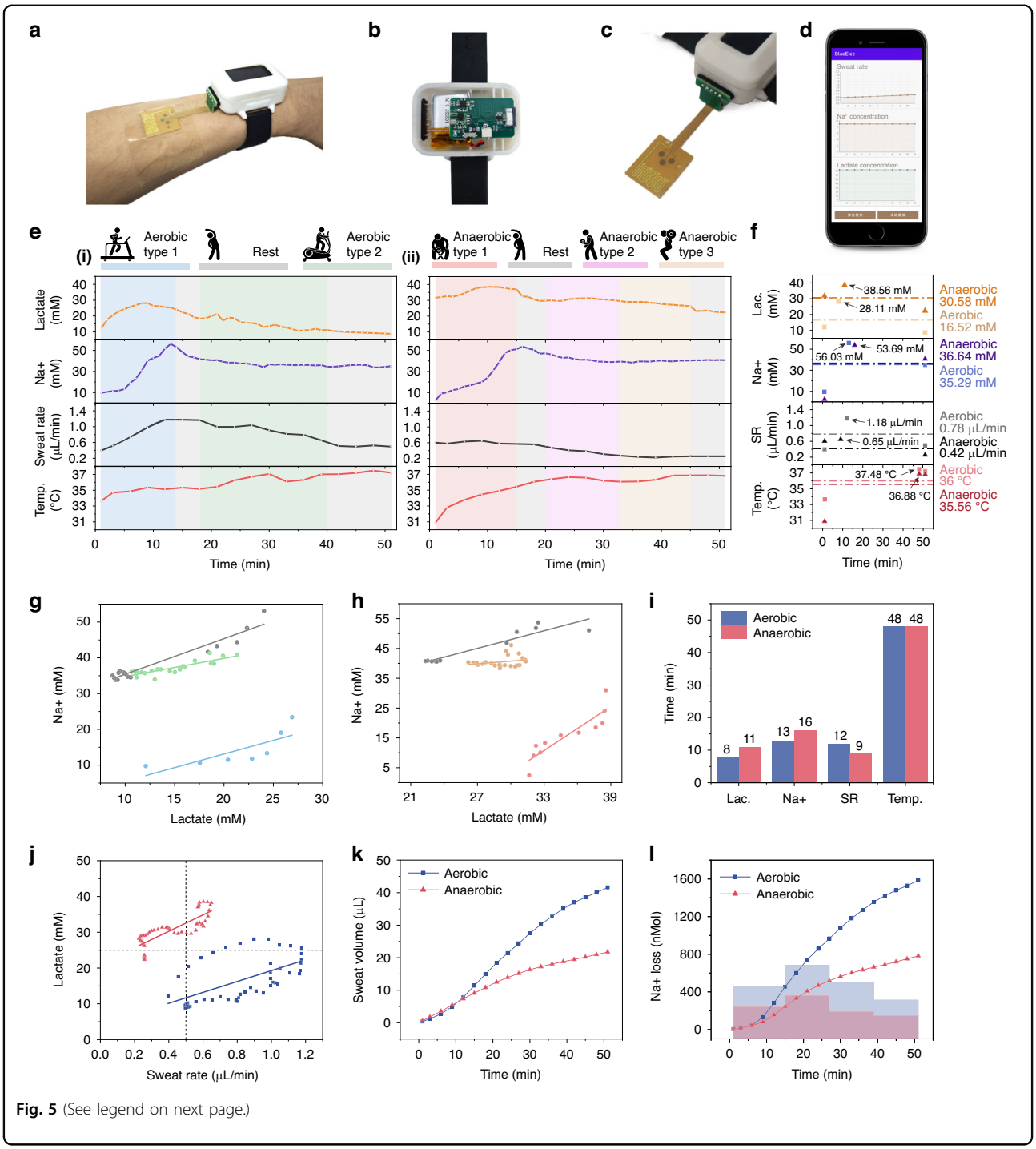

Fig. 5 (See legend on next page.)

values for 55 measurements at each of the six impedance values. Figure 4q presents the linear fitting results of the equivalent impedance values measured by the hardware system against the actual resistance values. The fitting curve equation is $y = 1.0041x + 0.01252$, achieving a linearity of $R^2 > 0.99$, fully demonstrating the accuracy and linear relationship of the impedance measurement.

Power consumption was further evaluated to assess the practical deployment capability of the wearable device. A 1 Ω sampling resistor was connected in series with the positive terminal of the lithium battery, and the voltage drop across the resistor was measured using a digital multimeter. The current consumption was calculated according to Ohm's law. Each operating mode was

(see figure on previous page)

Fig. 5 Individualized physiological profiling during aerobic and anaerobic exercises. a Image of the system worn on the arm. **b** Internal view of the hardware device. **c** Enlarged view of the magnetic interface connecting the hardware device to the FPCB-based sensing electrode. **d** Interface of the self-developed mobile APP, which receives data from the device via Bluetooth and displays and plots the data. **e** Real-time monitoring of sweat lactate concentration (yellow, 1-min interval), Na^+ concentration (blue, 1-min interval), sweat rate (black, 3-min interval), and body temperature (red, 3-min interval) during 51 min of aerobic exercise (i) and 51 min of anaerobic exercise (ii) after the onset of sweating. **f** Initial, peak, and final values of sweat lactate concentration (yellow dots), Na^+ concentration (blue dots), sweat rate (black dots), and body temperature (red dots) during 51 min of aerobic (light color) and anaerobic (dark color) exercises after the onset of sweating. Dashed lines indicate the average values of the four monitoring indicators. **g** Scatter distribution and fitting curves of Na^+ and lactate concentrations during 51 min of aerobic exercise, divided by exercise phases. Data from the first 8 min of aerobic training are shown in blue, data from the second aerobic phase (18–40 min) are shown in green, and data from the rest phases (13–18 min and 40–51 min) are shown in gray. **h** Scatter distribution and fitting curves of Na^+ and lactate concentrations during 51 min of anaerobic exercise, divided by exercise phases. Data from the first 11 min of anaerobic training are shown in red, data from the second and third anaerobic phases (20–45 min) are shown in yellow, and data from the rest phases (15–20 min and 45–51 min) are shown in gray. **i** Comparison of peak times for sweat lactate concentration, Na^+ concentration, sweat rate, and body temperature during aerobic (blue) and anaerobic (red) exercises. **j** Correlation plot between sweat rate (3-min interval) and lactate concentration (1-min interval) during aerobic (blue) and anaerobic (red) exercises. Missing sweat rate data points are filled using linear interpolation. Based on exercise intensity characteristics, the graph is divided into six regions: A (anaerobic zone), B1 (high-intensity anaerobic zone), B2 (high-intensity aerobic zone), C1 (low-intensity anaerobic zone), C2 (low-intensity aerobic zone), and D (aerobic zone). **k** Sweat loss during aerobic (blue) and anaerobic (red) exercises. (l) Na^+ loss during aerobic (blue) and anaerobic (red) exercises

recorded for 20 min using the MIN/MAX/AVG recording mode of the multimeter. The current consumption under three operating modes is shown in Fig. S18, and the detailed current records and estimated power consumption are summarized in Table 1. The average current was 13.2 mA in BLE advertising mode, 12.7 mA after BLE connection without sensing, and 13.5 mA under continuous sensing and BLE transmission. Under continuous sensing and BLE transmission, the estimated average power consumption was approximately 50.0 mW, calculated using the nominal battery voltage of 3.7 V. With a 500 mAh lithium battery, the estimated battery endurance was approximately 37.0 h under continuous operation. The battery voltage changed from 3.907 V to 3.877 V during the measurement, indicating stable power supply during the test. These results suggest that the wearable device can support long-term sweat monitoring during typical exercise sessions.

Practical human sweat detection

The practical human sweat detection study was approved by the Medical Ethics Committee of Tianjin Medical University General Hospital. Figure 5 demonstrates the application of the FPCB-based sweat detection system in real aerobic and anaerobic exercise scenarios. The wearable state of the device on the arm is shown in Fig. 5a. The device adopts a watch-like design, with the sensing electrodes reliably connected to the hardware system via magnetic interfaces. The FPCB-based sensing electrodes are fixed to the skin surface using adhesive, with perforations in the adhesive layer over the sweat pores to ensure smooth sweat excretion. Figure 5b presents the internal structure of the device, including the lithium battery that powers the system and the PCB board connected to the 5-pin magnetic interface via an FPC connector. Figure 5c provides an enlarged view of the connection, the electromechanical coupling between the FPCB sensors and the processing unit is secured via a 5-pin magnetic interface. The side view of the hardware device is shown in Fig. S19, with Fig. S19a displaying the Type-C interface for connecting the device to a host computer for debugging, and Fig. S19b showing the 5-pin magnetic interface for connecting to the sensing electrodes. Figure 5d illustrates the interface of the self-developed mobile APP, which wirelessly receives data from the hardware system via BLE module and enables real-time data display and plotting.

Longitudinal profiling of sweat biomarkers (lactate, Na +), sweat rate, and body temperature was conducted to validate the system's stability over extended durations. The stability of the electromechanical interconnection was specifically validated through this long-term on-body trial. Throughout the 51-min continuous monitoring session involving running and rapid arm swinging, the system maintained uninterrupted data transmission and stable baseline currents. The absence of significant motion artifacts or signal dropouts, which are typically associated with contact failure in modular connections, confirms the reliability of the rigid-flex architecture under dynamic physiological strain. Figure 5e presents the high-density temporal data acquired during aerobic (i) and anaerobic (ii) sessions. The system successfully captured the onset of sweating (defined as the 0-min mark) and maintained continuous operation for 51 min in both scenarios. Lactate and Na^+ concentrations are recorded at 1-min intervals, while sweat rate and body temperature are sampled every 3 min. Although the in vitro electrochemical calibrations were performed under controlled room-temperature conditions, the local temperature at the skin-adhered sensing interface during on-body exercise may differ from the in vitro condition. Future studies will incorporate temperature-dependent calibration and

compensation to further improve quantitative accuracy under real-world wearable conditions.

Since the equivalent impedance is set with an upper limit of 60 kΩ to ensure a sweat volume resolution of less than 0.69 μL, the resolution of sweat rate measurement reaches 0.23 μL/min when the sampling interval is set to 3 min. The 0-min mark represents the time point when the device successfully captures electrochemical data for lactate and Na^+ concentrations after sweating. Due to physiological differences between aerobic and anaerobic exercises, data collection begins at approximately 5 min for aerobic exercise and approximately 9 min for anaerobic exercise. From the successful data collection point, both exercises are monitored continuously for 51 min. During aerobic exercise, the subject first completes a 13-min segment, followed by a stretching break from 13 to 18 min, then a second aerobic segment from 18 to 40 min, and finally a second stretching break from 40 to 51 min. During anaerobic exercise, the subject completes the first segment before 15 min, takes a stretching break from 15 to 20 min, performs a second anaerobic segment from 20 to 33 min, continues without interruption into a third anaerobic segment from 33 to 45 min, and concludes with a second stretching break from 45 to 51 min. Figure 5f shows the initial, peak, and final values of sweat lactate concentration, Na^+ concentration, sweat rate, and body temperature during the 51-min aerobic (light color) and anaerobic (dark color) exercises, with dashed lines indicating the average values of the four monitoring indicators. Analysis of Fig. 5e and Fig. 5f reveals that exercise type significantly affects sweat composition and flow rate. For lactate concentration, both aerobic and anaerobic exercises show an initial increase followed by a decrease, but anaerobic exercise exhibits significantly higher lactate concentrations (average: 30.58 mM, maximum: 38.56 mM) compared to aerobic exercise (average: 16.52 mM, maximum: 28.11 mM). In contrast, the average and maximum Na^+ concentrations show no significant difference between the two exercise types. For sweat rate, the two exercise modes exhibit distinct trends. Aerobic exercise shows an initial increase followed by a decrease, while anaerobic exercise maintains a high initial rate that gradually declines. Notably, although the initial sweat rate of anaerobic exercise (0.60 μL/min) is higher than that of aerobic exercise (0.40 μL/min), its overall sweat rate is lower (anaerobic: average 0.42 μL/min, maximum 0.65 μL/min; aerobic: average 0.78 μL/min, maximum 1.18 μL/min). This phenomenon may be related to the longer time required for sweating during anaerobic exercise, resulting in a higher initial sweat rate but a lower overall flow rate. Body temperature gradually increases during both exercise types, with no significant difference in average or maximum temperatures, but the initial body temperature is lower for anaerobic exercise. Detailed initial, peak, final, and average values for sweat lactate concentration, Na^+ concentration, sweat rate, and body temperature for both exercise types are provided in Table S10.

During the 51-min aerobic exercise, the scatter distribution and fitting curves of sweat Na^+ concentration and lactate concentration are shown for different exercise phases (Fig. 5g). Since aerobic lactate peaks at 8 min and Na^+ concentration peaks at 13 min, data from the first 8 min of rising lactate and Na^+ concentrations are shown in blue; data from the second aerobic phase (18–40 min) are shown in green; and data from the two rest phases (13–18 min and 40–51 min) are shown in gray. The results indicate a correlation between lactate and Na^+ concentrations in each phase of aerobic exercise, with significant differences in concentrations between phases. While lactate concentration varies more widely within each aerobic phase, Na^+ concentration shows larger differences between aerobic phases, with higher concentrations in the second aerobic phase and rest phases compared to the first 8 min. Similarly, during the 51-min anaerobic exercise, the scatter distribution and fitting curves of sweat Na^+ concentration and lactate concentration are shown for different phases (Fig. 5h). Lactate peaks at 11 min and Na^+ concentration peaks at 16 min. Data from the first 11 min of rising lactate and Na^+ concentrations are shown in red; data from the second and third anaerobic phases (20–45 min) are shown in yellow; and data from the two rest phases (15–20 min and 45–51 min) are shown in gray. The lactate concentration during the initial 11-min anaerobic phase is notably higher than that in the second and third anaerobic phases, while the Na^+ concentration in the first 11 min is lower compared to the second, third anaerobic phases, and the recovery period. Additionally, the data points for the initial 11-min anaerobic phase are more dispersed, indicating greater variability in lactate and Na^+ concentrations during this stage. In contrast, the data points for the second and third anaerobic phases are the most densely clustered, suggesting minimal fluctuations in sweat lactate and Na^+ concentrations during these periods. Figure 5i compares the peak times of sweat lactate concentration, Na^+ concentration, sweat rate, and body temperature during aerobic and anaerobic exercises. Lactate, Na^+, and sweat rate peak earlier in aerobic exercise, while body temperature peaks later. Lactate and Na^+ peak earlier in aerobic exercise, while sweat rate peaks earlier in anaerobic exercise.

This study investigates the relationship between sweat rate and lactate concentration during aerobic and anaerobic exercises, proposing a two-parameter method for interpreting exercise intensity based on their joint detection. Figure 5j illustrates the distribution of sweat rate and lactate concentration during aerobic (blue) and anaerobic

(red) exercises. Sweat lactate was used as a metabolic-related indicator during exercise, while sweat rate reflected exercise-induced sweating and fluid loss. Based on these two parameters, the exercise process was divided into different intensity zones to provide a more intuitive interpretation of the on-body sweat profiles. In this work, the thresholds were derived from the observed distribution of the single-subject exercise data. Therefore, the zoning model is intended as a proof-of-concept and subject-specific analysis method, rather than a universal exercise intensity classification standard.

Missing data points, resulting from the 3-min sweat rate sampling interval and 1-min lactate sampling interval, were interpolated using linear interpolation. Lactate concentration and sweat rate thresholds of 25 mM and 0.5 μL/min, respectively, were used to divide the graph into four primary regions (A–D). Further segmentation along the diagonal direction allowed the identification of six zones: A (anaerobic zone), B1 (high-intensity anaerobic zone), B2 (high-intensity aerobic zone), C1 (low-intensity anaerobic zone), C2 (low-intensity aerobic zone), and D (aerobic zone). Most anaerobic exercise data points were distributed in Zone A, which was characterized by high sweat lactate concentration and low sweat rate. In contrast, aerobic exercise data points were mainly concentrated in Zone D, which showed low sweat lactate concentration and high sweat rate. Data points in Zone C, with low sweat lactate concentration and low sweat rate, were associated with low-intensity exercise, while data points in Zone B, with high sweat lactate concentration and high sweat rate, were associated with high-intensity exercise. The diagonal division further helped separate aerobic and anaerobic states within these transition regions.

The combined analysis of lactate, Na^+, and sweat rate provides complementary physiological information for individualized exercise assessment. Sweat lactate mainly reflects exercise-related metabolic stress and glycolytic activity, while sweat rate reflects thermoregulatory sweating and sweat gland activity. In addition, sweat Na^+ concentration is closely related to electrolyte loss, and its combination with sweat rate enables the estimation of dynamic Na^+ loss during exercise. Therefore, these three parameters together describe metabolic response, fluid loss, and electrolyte loss. Compared with a single sweat biomarker, this multi-parameter profile provides a more comprehensive view of the exercise process and helps support personalized interpretation of exercise status and hydration demand.

Beyond instantaneous biomarker levels, the platform also enabled cumulative loss analysis. Figure 5k shows the dynamic accumulation of total sweat volume during exercise. The results showed that the cumulative sweat loss gradually diverged between aerobic and anaerobic exercise. Aerobic exercise led to higher cumulative sweat loss, which may be related to sustained thermoregulatory demand. By combining real-time Na^+ concentration with sweat rate, the total Na^+ loss was further estimated, as shown in Fig. 5l. The cumulative Na^+ loss showed a similar divergence trend, with aerobic exercise resulting in greater total electrolyte loss. To further analyze the temporal characteristics of electrolyte loss, the 51-min monitoring period was divided into four phases: 0–15, 15–27, 27–39, and 39–51 min. The phase-resolved analysis showed that Na^+ loss reached a peak during the 15–27 min interval for both exercise types, followed by a gradual decrease in the later phase. These results suggest that the simultaneous monitoring of sweat rate and Na^+ concentration can provide useful information for individualized fluid and electrolyte replenishment during exercise.

In addition to sensing performance during exercise, wearing comfort and skin compatibility are also important for practical wearable applications[46]. In this work, the FPCB sensor was fabricated on a thin PI substrate, the microfluidic patch was fabricated using M-FC photocurable resin with a MakeX M-One Pro 30 DLP 3D printer, and skin attachment was achieved using a commercial PU-film medical adhesive tape (Shanghai Hons Medical Technology Co., Ltd., China), as shown in Fig. S18a and Fig. S18b. PI films have been widely used in flexible electronic devices because of their flexibility, chemical stability, and mechanical robustness[47]. Gold-based conductive materials are also commonly used in bioelectronic and wearable sensing interfaces because of their good conductivity, chemical stability, and reported biocompatibility[48]. In addition, PU-film medical adhesive tapes are widely used for skin-contact fixation in wound dressings, wearable sensors, and medical patches[49]. These material features provide a basis for the use of this sensing front-end in short-term wearable applications.

To preliminarily evaluate wearing comfort, the assembled sensing front-end was attached to the forearm skin for 4 h using the medical adhesive tape (Fig. S18c). Skin appearance was recorded before attachment (Fig. S18d), immediately after removal (Fig. S18e), and 30 min after removal (Fig. S18f). As shown in Fig. S18e and Fig. S18f, no obvious redness, swelling, discoloration, or skin damage was observed after removal, and the slight indentation caused by short-term attachment largely disappeared after 30 min. No itching, pain, or burning sensation was reported during the test. These results provide preliminary evidence for short-term wearing comfort. However, this observation cannot replace standardized skin irritation, sensitization, or cytotoxicity tests, and longer-term skin compatibility still requires further evaluation.

To further highlight the engineering features of the present platform, representative wearable sweat sensing

Table 2 Comparison of representative wearable sweat sensing systems

Reference	Analytes	Electrode substrate	Replaceable sensing front-end	Repeated plug-in test	Other reliability evaluation
Yin et al.[1]	Glucose, lactate, Na^+, pH	Screen-printed Ag/carbon electrodes	Not emphasized	Not reported	Stretching and wearing stability
Xu et al.[8]	Lactate, EEG, EOG, EDA	Printed Ag/PB electrodes	Not emphasized	Not reported	In-ear signal monitoring
Shen et al.[38]	β-HB	Screen-printed carbon electrodes	Not emphasized	Not reported	On-body monitoring
Liu et al.[40]	Na^+, K^+	PCB-ENIG electrodes	Not emphasized	Not reported	Ion-sensing repeatability
Komkova et al.[44]	Lactate, sweat secretion rate	Screen-printed carbon/silver electrodes	Partially	Not reported	On-body monitoring
This work	Lactate, Na^+, sweat rate	FPCB-ENIG electrodes	Yes	1–300 cycles	Contact resistance, dynamic bending, artificial sweat immersion, and on-body monitoring

systems were compared in Table 2. The comparison focuses on sensing targets, electrode substrate, replaceable sensing front-end design, repeated plug-in testing, and reliability evaluation. Recent studies have demonstrated substantial progress in wearable sweat sensing systems, including advances in flexible electrode fabrication, multimodal biomarker monitoring, device integration, and sweat sampling strategies. However, repeated plug-in reliability between a replaceable sensing front-end and an electronic module has rarely been reported. In this work, the FPCB is not only used as a flexible electrode substrate, but also as a mechanically reinforced plug-and-play sensing front-end. The ENIG contact terminals and PI-stiffened connection region provide a stable electrical interface with the wearable electronics. Together with contact resistance measurement, dynamic bending, 1–300 plugging/unplugging cycles, artificial sweat immersion, and on-body exercise monitoring, these results suggest that the proposed FPCB interconnection strategy can provide a practical engineering route for improving the reliability of wearable sweat analysis systems.

Conclusions

In summary, a scalable and mechanically robust sweat analysis platform has been developed leveraging FPCB technology. A unique hierarchical electrode architecture was established, wherein the industrial ENIG layer functions as a high-precision current collector and the surface-modified carbon layer serves as a corrosion-resistant transducer. To address the physical vulnerabilities of conventional soft sensors, the platform utilizes PI-stiffened ENIG gold fingers. This robust plug-and-play interface effectively eliminates motion artifacts and severe signal attenuation during dynamic exercise.

CA is employed for lactate sensing and the electrode surface is functionalized to achieve a wide detection range of 5 mM–80 mM, with a sensitivity of 0.4046 μA/Lac(mM). For Na^+ sensing, OCP is utilized, with a detection range of 12.5 mM–200 mM and a sensitivity of 119.59 mV/lg([Na^+]/mM). Additionally, the system achieves high-precision measurement with sweat volume resolution below 0.69 μL and flow rate resolution below 0.23 μL/min. In terms of hardware system performance verification, this study systematically evaluates measurement errors. Within the tested detection range, the system error of CA detection is controlled within 2.46%, the device error of OCP measurement is below 5.24%, and the system error of equivalent impedance measurement is controlled within 5.89%. Beyond hardware optimization, a proof-of-concept framework for personalized exercise intensity zoning was demonstrated. By performing multi-parameter fusion analysis of sweat rate and lactate concentration, a six-zone intensity model (Anaerobic A to Aerobic D) was constructed based on individual

physiological thresholds. This approach offers a quantifiable method to differentiate aerobic and anaerobic states, shifting the paradigm from generic population standards to precision subject-specific assessment. Additionally, by analyzing sweat flow rate and Na^+ concentration, the system can monitor sweat loss and Na^+ loss during exercise in real time, providing scientific references for hydration and electrolyte replenishment.

While this work establishes a solid technical pathway for mass-producible wearable sensors, certain limitations remain. The current microfluidic module utilizes 3D printing for rapid validation, which will be transitioned to injection molding in future mass-production iterations. Additionally, the exercise zoning model presented here is based on a longitudinal pilot study of a single subject. Future research will prioritize large-scale clinical trials to develop robust, population-level calibration algorithms and further validate the universality of this personalized profiling strategy.

Supporting Information

Technical Details and Experimental Methods; processes of the electrochemical sensing modules; the integration workflow of the microfluidic chip; and the circuit design details of the custom-developed potentiostat hardware.

Acknowledgements
The authors gratefully thank financial assistance from the Project of Cultivation for young top-motch Talents of Beijing Municipal Institutions (BPHR202203229), the National Natural Science Foundation of China (61805016;81402391), National key R&D program of China (2022YFB3203700).

Author details
[1]School of Instrument Science and Optoelectronic Engineering, Beijing Information Science and Technology University, Beijing, China. [2]Department of Clinical Laboratory, Tianjin Medical University General Hospital, Tianjin, China. [3]Research Center for Materials Science and Opti-Electronic Technology, School of Optoelectronics, University of Chinese Academy of Sciences, Beijing, China. [4]Research Center for Materials Science and Opti-Electronic Technology, College of Materials Science and Opti-Electronic Technology, University of Chinese Academy of Sciences, Beijing, China

Author contributions
Investigation, formal analysis, data curation, writing—original draft: TX; methodology, writing—review & editing, Visualization: TX and GZ; Review: TX, WL, JZ, CL and BL; supervision: JTL, CJC and GZ; funding acquisition: GZ.

Conflict of interest
The authors declare no competing interests.

Supplementary information The online version contains supplementary material available at https://doi.org/10.1038/s41378-026-01436-5.

Received: 6 May 2026 Revised: 9 July 2026 Accepted: 21 July 2026
Published online: 16 September 2026

References

1. Yin, L. et al. A stretchable epidermal sweat sensing platform with an integrated printed battery and electrochromic display. *Nat. Electron.* **5**, 694–705 (2022).
2. Ye, C. et al. A wearable aptamer nanobiosensor for non-invasive female hormone monitoring. *Nat. Nanotechnol.* **19**, 330–337 (2024).
3. Yang, Y. et al. A laser-engraved wearable sensor for sensitive detection of uric acid and tyrosine in sweat. *Nat. Biotechnol.* **38**, 217–224 (2020).
4. Ding, S. et al. A fingertip-wearable microgrid system for autonomous energy management and metabolic monitoring. *Nat. Electron.* **7**, 788–799 (2024).
5. Min, J. et al. Continuous biochemical profiling of the gastrointestinal tract using an integrated smart capsule. *Nat. Electron.* **8**, 844–855 (2025).
6. Ye, S. et al. Recent progress in wearable biosensors: from healthcare monitoring to sports analytics. *Biosensors* **10**, 205 (2020).
7. Kim, S.-R. et al. Electrodermal activity as a proxy for sweat rate monitoring during physical and mental activities. *Nat. Electron.* **8**, 353–361 (2025).
8. Xu, Y. et al. In-ear integrated sensor array for the continuous monitoring of brain activity and of lactate in sweat. *Nat. Biomed. Eng.* **7**, 1307–1320 (2023).
9. Senf, B. et al. Recent advances in portable biosensors for biomarker detection in body fluids. *Biosensors* **10**, 127 (2020).
10. Bariya, M., Nyein, H. Y. Y. & Javey, A. Wearable sweat sensors. *Nat. Electron.* **1**, 161–171 (2018).
11. Derbyshire, P. J., Barr, H., Davis, F. & Higson, S. P. J. Lactate in human sweat: a critical review of research to the present day. *J. Physiol. Sci.* **62**, 429–440 (2012).
12. He, W. et al. Integrated textile sensor patch for real-time and multiplex sweat analysis. *Sci. Adv.* **5**, eaax0649 (2019).
13. Kim, J., Campbell, A. S., De Ávila, B. E.-F. & Wang, J. Wearable biosensors for healthcare monitoring. *Nat. Biotechnol.* **37**, 389–406 (2019).
14. LeGrys, V. A., Yankaskas, J. R., Quittell, L. M., Marshall, B. C. & Mogayzel, P. J. Diagnostic sweat testing: the cystic fibrosis foundation guidelines. *J. Pediatr.* **151**, 85–89 (2007).
15. Mattar, A. C. V., Leone, C., Rodrigues, J. C. & Adde, F. V. Sweat conductivity: an accurate diagnostic test for cystic fibrosis? *J. Cyst. Fibros.* **13**, 528–533 (2014).
16. Raina, M. A. et al. Assessment of correlation between sweat chloride levels and clinical features of cystic fibrosis patients. *J. Clin. Diagn. Res. JCDR* **10**, BC01–BC06 (2016).
17. Jia, W. et al. Electrochemical tattoo biosensors for real-time noninvasive lactate monitoring in human perspiration. *Anal. Chem.* **85**, 6553–6560 (2013).
18. Biagi, S., Ghimenti, S., Onor, M. & Bramanti, E. Simultaneous determination of lactate and pyruvate in human sweat using reversed-phase high-performance liquid chromatography: a noninvasive approach. *Biomed. Chromatogr.* **26**, 1408–1415 (2012).
19. Buono, M. J., Lee, N. V. L. & Miller, P. W. The relationship between exercise intensity and the sweat lactate excretion rate. *J. Physiol. Sci.* **60**, 103–107 (2010).
20. Seki, Y. et al. A novel device for detecting anaerobic threshold using sweat lactate during exercise. *Sci. Rep.* **11**, 4929 (2021).
21. Li, H. et al. Personalized hydration strategy to improve fluid balance and intermittent exercise performance in the heat. *Nutrients* **16**, 1341 (2024).
22. Sun, Z. et al. Conducting polymer hydrogels based on supramolecular strategies for wearable sensors. *Exploration* **4**, 20220167 (2024).
23. Yang, M. et al. Advances in non-electrochemical sensing of human sweat biomarkers: from sweat sampling to signal reading. *Biosensors* **14**, 17 (2024).
24. Baker, L. B. Sweating rate and sweat sodium concentration in athletes: a review of methodology and intra/interindividual variability. *Sports Med. Auckl. Nz* **47**, 111–128 (2017).
25. Gao, F. et al. Wearable and flexible electrochemical sensors for sweat analysis: a review. *Microsyst. Nanoeng.* **9**, 1 (2023).
26. Wang, Z. et al. Engineering materials for electrochemical sweat sensing. *Adv. Funct. Mater.* **31**, 2008130 (2021).
27. Mohan, A. M. V., Rajendran, V., Mishra, R. K. & Jayaraman, M. Recent advances and perspectives in sweat based wearable electrochemical sensors. *TrAC Trends Anal. Chem.* **131**, 116024 (2020).
28. Bilbao, E. et al. Electrochemical sweat sensors. *Chemosensors* **11**, 224 (2023).
29. Amjad, A. & Xian, X. Optical sensors for transdermal biomarker detection: a review. *Biosens. Bioelectron.* **267**, 116844 (2025).
30. Zhong, B. et al. Monolithic cell-on-memristor architecture enables wafer-scale integration of oscillatory chemoreceptors for bio-realistic gustatory chips. *Nat. Mater.* **25**, 275–284 (2026).
31. Zheng, Y. et al. Twelve-inch electrically anisotropic boridene for optoelectronic computing. *Nat. Nanotechnol.* **21**, 571–578 (2026).
32. Li, Z. et al. A reconfigurable heterostructure transistor array for monocular 3D parallax reconstruction. *Nat. Electron.* **8**, 46–55 (2025).
33. Zhao, P. et al. A time sequential microfluid sensor with Tesla valve channels. *Nano Res* **16**, 11667–11673 (2023).

34. Wang, M. et al. A wearable electrochemical biosensor for the monitoring of metabolites and nutrients. *Nat. Biomed. Eng.* **6**, 1225–1235 (2022).
35. Wang, M. et al. Printable molecule-selective core–shell nanoparticles for wearable and implantable sensing. *Nat. Mater.* **24**, 589–598 (2025).
36. Wang, C. et al. A microfluidic wearable device for wound exudate management and analysis in human chronic wounds. *Sci. Transl. Med* **17**, eadt0882 (2025).
37. Evert, B., Peterson, K. L., Songkakul, T., Bozkurt, A. & Daniele, M. A. Multimodal wearable platform with simultaneous electrochemical and biophotonic sensing. *ACS Sens* **10**, 5495–5507 (2025).
38. Shen, Y. et al. Wearable microfluidic electrochemical sensor integrated with iontophoresis for non-invasive sweat ketone monitoring. *Sens. Actuators B Chem.* **421**, 136518 (2024).
39. Dutta, G., Regoutz, A. & Moschou, D. Enzyme-assisted glucose quantification for a painless lab-on-PCB patch implementation. *Biosens. Bioelectron.* **167**, 112484 (2020).
40. Liu, H. et al. Printed circuit board integrated wearable ion-selective electrode with potential treatment for highly repeatable sweat monitoring. *Sens. Actuators B Chem.* **355**, 131102 (2022).
41. Mansor, A. F. M. et al. Gold-coated impedance biosensors on PCB and PET for real-time monitoring of cancer cells. *ECS Sens.* **3**, 042401 (2024).
42. Nandeshwar, R. & Tallur, S. Electrochemical detection of myeloperoxidase (MPO) in blood plasma with surface-modified electroless nickel immersion gold (ENIG) printed circuit board (PCB) electrodes. *Biosens. Bioelectron.* **246**, 115891 (2024).
43. Evans, D. et al. A novel microfluidic point-of-care biosensor system on printed circuit board for cytokine detection. *Sensors* **18**, 4011 (2018).
44. Komkova, M. A. et al. Simultaneous monitoring of sweat lactate content and sweat secretion rate by wearable remote biosensors. *Biosens. Bioelectron.* **202**, 113970 (2022).
45. Patterson, M. J., Galloway, S. D. R. & Nimmo, M. A. Variations in regional sweat composition in normal human males. *Exp. Physiol.* **85**, 869–875 (2000).
46. Heikenfeld, J. et al. Wearable sensors: modalities, challenges, and prospects. *Lab. Chip* **18**, 217–248 (2018).
47. Lin, J. et al. Applications of flexible polyimide: barrier material, sensor material, and functional material. *Soft Sci.* **3**, 2 (2023).
48. Vafaiee, M., Vossoughi, M., Mohammadpour, R. & Sasanpour, P. Gold-plated electrode with high scratch strength for electrophysiological recordings. *Sci. Rep.* **9**, 2985 (2019).
49. He, X. et al. Adhesive tapes: from daily necessities to flexible smart electronics. *Appl. Phys. Rev.* **10**, 011305 (2023).